Discovering Motifs in Ranked Lists of DNA Sequences

Eran Eden

Discovering Motifs in Ranked Lists of DNA Sequences

Research Thesis

Submitted in partial fulfillment of the requirements
for the degree of Master of Science in Computer Science

Eran Eden

Submitted to the Senate of
the Technion — Israel Institute of Technology

SHVAT 5767 Haifa January 2007

This research thesis was done under the supervision of Dr. Zohar Yakhini in the Computer Science department. First and foremost I would like to thank Zohar for his dedicated guidance and assistance. I also wish to acknowledge the contribution of Doron Lipson and Sivan Yogev to this study as well as the assistance of Mark Silberstein in connecting the DRIM application to the Condor computer grid.

The generous financial help of the Technion as well as that of the Gutwirth fellowship is gratefully acknowledged.

Contents

1 Abstract **1**

2 Abbreviations **2**

3 Introduction **3**

3.1 Background . . . 3

3.1.1 Motif representations . . . 3

3.1.2 Background models . . . 4

3.1.3 Motif enrichment scores . . . 5

3.1.4 Scanning the motif space . . . 5

3.2 Open challenges in motif discovery . . . 6

3.3 Data lends itself to ranking in a natural manner . . . 7

3.4 Overview . . . 9

4 Materials and Methods **10**

4.1 The minimum hyper-geometric (mHG) score . . . 10

4.2 Calculating the p-value of the mHG score . . . 11

4.3 Multi-dimensional mHG Score . . . 12

4.3.1 P-value of the multi-dimensional mHG score . . . 14

4.4 Partition-limited mHG score . . . 14

4.5 The DRIM Software . . . 15

4.5.1 Work-flow . . . 16

4.5.2 How to compute the mHG score efficiently . . . 18

4.5.3 How to compute the mHG p-value efficiently . . . 19

4.5.4 Optimizing the occurrence vector generation . . . 21

4.5.5 Measuring motif similarity . . . 21

4.6 Characteristics of data sets . . . 22

4.6.1 ChIP-chip dataset . . . 22

4.6.2 Methylated CpG dataset . . . 24

5 Results **25**

5.1 Proof of principle . . . 25

5.2 TFBS prediction in yeast using ChIP-chip data . . . 26

5.2.1 Aro80 transcription regulatory network . . . 27
5.2.2 CA repeats are correlated with TF binding . . . 30
5.2.3 Detection of indirect TF-DNA binding using ChIP-chip . . . 31
5.2.4 Condition dependent motifs . . . 33
5.3 Motif discovery in Human methylated CpG islands . . . 34
5.4 Motif discovery in Human ChIP-chip data . . . 35
5.5 Comparison to other methods . . . 37
5.5.1 Dynamic vs. rigid cutoffs . . . 37
5.5.2 Controlling false positives . . . 38
5.5.3 Binary versus multi-dimensional enrichment . . . 38

6 Discussion **39**
6.1 Addressing the four challenges of motifs discovery and future challenges . . . 40
6.2 Sequence length bias in ChIP-chip data . . . 41
6.3 Novel motifs in ChIP-chip data . . . 42
6.4 Novel motifs in CpG data . . . 42
6.5 Concluding remarks . . . 43

References **43**

7 Appendix I - Supplementary material **48**
7.1 Bounds for the mHG p-value . . . 48
7.2 How to compute the mHG score efficiently on trinary vectors . . . 49
7.3 Comparing mHG and HG on simulated motif occurrences . . . 50
7.4 Hypothesis: Aro80 network is inhibited by GATA binding factors . . . 50
7.5 mHG and GO analysis . . . 51
Table S1 . . . 55
Table S2 . . . 59
Table S3 . . . 65
Table S4 . . . 66

8 Appendix II - List of publications (during M.Sc. period): **67**

9 Appendix III - Web servers and software (during M.Sc. period): **67**

List of Figures

1 DRIM flow chart. DRIM receives a list of DNA sequences as input and a criterion by which the sequences should be ranked, for example TF binding signals as measured by ChIP-chip, and performs the following steps: (i) The sequences are ranked according to the criterion. (ii) A "blind search" is performed over all the motifs that reside in the restricted motif space (in this study the restricted motif space contains $\sim$ 100,000 motifs, see Section 4.5). For each motif an occurrence vector is generated. Each position in the vector is the number of motif occurrences in the corresponding sequence, (the figure shows the vector for the motif CACGTGW). (iii) The motif significance is computed using the mHG scheme, and the optimal partition into target and background sets in terms of motif enrichment is identified. The promising motif seeds are passed as input to the heuristic motif search model and the rest are filtered out. (iv,v) The motif seeds are expanded in an iterative manner, (the mHG is computed in each lap) until a local optimum motif is found. (vi) The exact mHG p-value of the motif is computed. If it has a p-value $< 10^{-3}$ then it is predicted as a true motif (the choice of this threshold is explained in Section 5.1). The output of the system is the motif representation above IUPAC, its PSSM, mHG p-value and optimal set partition cutoff. 8

2 The two-dimensional grid used for calculating the mHG p-value. In this example $N = 30$, $B = 10$, $W = 20$ and $p = 0.1$. Light blue area describes all attainable values of w and b. Red area describes the subset R: all values of w and b for which HGT$(b; N, B, n) \leq p$, where $n = w + b$. Two $(0, 0) \rightarrow (N, B)$ paths are depicted, representing the binary label vectors $\lambda_1 = \{1,0,1,1,0,0,0,1,1,1,1,1,0,1,0,0,0,0,0,0,0,0,0,0,0,1,0,0,0\}$ and $\lambda_2 = \{0,0,1,0,0,0,0,1,0,0,0,0,0,1,1,1,0,1,0,0,0,0,0,0,0,1,1,1,0,1\}$. The path λ_1 traverses R, demonstrating that mHG$(\lambda_1) \leq p$. The path λ_2 does not traverse R, demonstrating that mHG$(\lambda_2) > p$. The mHG p-value is calculated by counting all the paths from (0,0) to (W,B) that do not visit R divided by the total number of paths and subtracting this from 1. 12

3 The 3-dimensional grid used for calculating the 3-dimensional mHG p-value. Given W, B, Y and p one can compute the region R (red region in the figure): the subset of all points (w,b,y) in the grid for which HGT$(b, y; N, B, n) \leq p$, where $n = w + b + y$ and $N = W + B + Y$. Two $(0, 0, 0) \rightarrow (W, B, Y)$ paths are depicted. The path λ_1 traverses R, demonstrating that mHG$(\lambda_1) \leq p$. The path λ_2 does not traverse R, demonstrating that mHG$(\lambda_2) > p$. The mHG p-value is calculated by counting all the paths from (0,0,0) to (W,B,Y) that do not visit R divided by the total number of paths, and subtracting this from 1. 15

4 The two-dimensional grid used for calculating the partition limited mHG p-value. In this example $N = 30$, $B = 10$, $W = 20$, $p = 0.1$ and $n_{max} = 14$. The red area describes the subset R: all values of w and b for which HGT$(b; N, B, n) \leq p$, and $n = w + b \leq n_{max}$. The light blue area describes all attainable values of w and b. The partition limited mHG p-value is calculated by counting all the paths from (0,0) to (W,B) that do not visit R divided by the total number of paths, and subtracting this from 1. 16

5 The distribution of TFBS occurrence multiplicities per intergenic region in Saccharomyces cerevisiae is shown for five TFs whose TFBS motif was experimentally verified. Note that the y-axis is logarithmic and that the fraction of sequences with 3 or more occurrences is less than 0.1%. 18

6 HGT scores over all possible 15 partitions of a given vector $\lambda = (0, 0, 0, 0, 1, 0, 0, 1, 0, 0, 0, 1, 0, 0, 0)$. The local minima HGT scores are achieved in partitions n=5,8,12 where $\lambda(5) = \lambda(8) = \lambda(12) = 1$. 20

7 A summary of the location analysis (ChIP - chip) procedure 23

8 Sequence length bias observed in ChIP-chip data of the TF MSN2 measured in an acidic condition. The yeast intergenic regions were ranked according to their binding to MSN2, (strong to weak binding appear from left to right). The figure shows the sequence lengths at each rank. The red trend line (a moving average of 200) indicates that sequences that are ranked higher in terms of TF binding are also longer. A student t-test comparing the lengths of the top 300 versus the rest of the sequences yielded a highly significant p-value $\leq 10^{-40}$. . . . 24

9 Comparison of mHG score and p-value distributions for motifs in randomly ranked sequences with those of true TFBS motifs in ranked lists derived from the corresponding ChIP-chip assays. $\sim$100,000 motifs were scanned in 400 randomly ranked genomic sequences, and their corresponding corrected p-value (a) and mHG score (b) were recorded. The corrected p-values involves two levels of multiple test corrections: correction on the number of motifs that were tested and correction for the multiple cutoffs that are tested as part of the mHG optimization process. None of the tested motifs had a corrected p-value$<10^{-3}$. DRIM was applied on the ChIP-chip data of 5 TFs and the mHG scores and corrected p-values of the true TFBS motifs (as previously determined experimentally) were recorded. In all instances the true TFBS motifs were predicted with p-values that were several orders of magnitude more significant than the best random set motif p-value. 26

10 Comparison between predictions of DRIM and published predictions of 6 other methods and conservation data as reported in [1]. Overall, out of 162 unique TFs, DRIM identified significant motifs for 82 TFs with p-value$<10^{-3}$. Out of the 162 TFs, DRIM and the other applications agree on 96 TFs: 27 TFs for which a similar motif was found and 69 TFs for which no significant motifs were found. There are 5 TFs for which the motifs predicted by DRIM and other applications differ; 11 for which the other applications identified motifs that DRIM did not and 50 for which DRIM identified a motif that the other applications did not (for details see Supplementary Table S2 and Table S3). Sequence logos were generated using the *RNA Structure Logo* software [2]. 27

11 The hypothetical regulatory network of Aro80. Copies of the BS_{Aro80} motif (on the sense and anti sense) are shown as rectangles on the promoter regions. (a) BS_{Aro80} is conserved in 4 strains of yeast as shown using the UCSC browser conservation plots. Aro80 regulates the utilization of secondary nitrogen sources such as aromatic amino acids by binding genes that participate in the catabolism of aromatic amino acids. We hypothesize that it also binds to its own promoter region and introduces a positive feedback self loop. (b) Part of the Aro80 promoter sequence is shown with bases of the BS_{Aro80} motif colored in red. Interestingly, there are three GATA binding sites that are adjacent to the BS_{Aro80} motif (bases colored in green). These sites bind GATA factors that are known to play a role in nitrogen catabolite repression. We hypothesize that they are also involved in the repression of Aro80 expression by physically binding to the region near BS_{Aro80} thus making it inaccessible to Aro80 binding. This in turn breaks the positive feedback loop and represses the expression of Aro80 itself and other Aro80 regulated genes. 30

12 Compatibility between the BS_{Aro80} motif identified by DRIM and previously reported mutagenesis studies [3]. The Aro9 promoter region from base -169 to -133 as well as 6 other copies containing mutations and deletions are shown. These regions were used in order to construct hybrid promoters and measure the expression of a reporter gene, which is dependent on the binding of Aro80 to the promoter[3]. The two partially overlapping copies of BS_{Aro80} that reside in the Aro9 promoter and an additional sequence element that is similar to the canonic BS_{Aro80} (2 different bases) are marked with green and blue arrows respectively. It can be seen that the expression values can be explained in terms of intact BS_{Aro80} copies, i.e more intact copies yield higher expression. 31

13 Visualization of CA repeat occurrences in the yeast genome and their correlation with TF binding. $\sim$6000 intergenic regions were ranked according to their binding to the TF AFT2 in a H_2O_2Hi ChIP-chip experiment [1] and the motif CACACACA was searched in each of the regions. On the left is the motif *occurrence vector* with white, black, blue and red lines indicating whether the corresponding region contains 0, 1, 2 or $>$2 motif occurrences respectively. It can be seen that the top of the vector is significantly more dense than the rest of the vector indicating that the CA repeats are highly correlated with AFT2 binding. In the center is the *motif occurrence map* in which the blue lines mark the bases of the motif occurrences. It can be seen that that the density of motif occurrences increases in regions that are ranked high in the list . On the right is a plot of the expected vs. observed cumulative motif occurrences. The x-axis represents the ranked intergenic regions and the y-axis is the cumulative motif occurrence as function of rank. The height of the y-axis is the total number of motif occurrences. 32

14 (a) Schematic representation of Met4-Met28-CBF and Met4-Met28-Met31/32 complexes [4, 5]. (b) A hypothetical Met4-Met28-CBF-Met31/32 complex. Immuno-precipitation of any of the TFs in the complex will precipitate the same set of sequences, which explains why DRIM identifies the same two motifs for all TFs in the complex. 33

15 Occurrences of CA repeats in the human genome and their correlation to CpG methylation. (a) $\sim$13,000 promoters were ranked according to their CpG methylation in a human carcinoma cell-line [6]. Similarly to Figure 13 from left to right are the *occurrence vector*, *motif occurrence map* and the plot of the *cumulative motif occurrence*, all generated for the motif CACACACA. It can be seen that the CA repeats are highly correlated with CpG methylation as indicated by the increased density of the motif occurrences at the regions that are ranked top. (b) A control experiment in which the promoters are randomly ranked. It can be seen that the CA repeat occurrences are distributed uniformly and the observed cumulative motif occurrence is close to the expected. . 36

16 Comparison between HG and mHG enrichment. The mHG and HG methods were applied to ChIP-chip data of 6 TFs. The sequences were ranked according to the ChIP-chip binding signal and the enrichment of the correct binding motif was recorded using mHG and HG with fixed target sets containing the top 10, 100, 1000 sequences as well as all sequences with ChIP-chip signal $< 10^{-3}$. All scores were corrected for multiple motif testing. The mHG score is also corrected for the multiple cutoff testing. The 10^{-3} and mHG cutoffs for each experiment are shown. It can be seen that the two cutoffs are significantly different and that for all the tested TFs mHG produces better results than HG in terms of enrichment of the true motif. 38

17 Comparison of the target sets sizes as determined by the fixed versus the mHG flexible cutoffs. Each dot represents a ChIP-chip experiment where the x and y coordinates are the number of promoters with $p < 10^{-3}$ (standard cutoff) and the number of promoters as determined by the mHG cutoff, respectively. The dotted line is $x = y$. TF names are given in Table S4 39

18 Motif occurrences in the top 59 (of $\sim$6000) promoters that were ranked according to Met32 binding signal. A comparison is made between the data driven mHG cutoff and the arbitrary fixed cutoff. It can be seen that the motifs are significantly more enriched when the list is partitioned using the mHG cutoff. 40

S1 Comparison of p-value bounds, exact p-value calculation and observed frequencies of mHG scores for two synthetic cases: a) $N = 600$, $B = 300$, b) $N = 330$, $B = 30$. In each case the following values were generated for several different mHG scores: lower bound (p), trivial upper bound (Np), tighter upper bound(Bp), exact p-value calculation (pVal) and observed p-values over 10,000 random instances (sim). Note the improvement of the tighter upper bound (Bp) when $N >> B$. 49

S2 Comparison of the mHG and HG methods on simulations of motif occurrence vectors. The vectors were generated according to a rank dependent distribution (Section 7.3) with 18 different parameter combinations ($a = 10, 50, 100; b = 0.01, 0.05, 0.1; u = 0.01, 0.1$). The -log fraction between mHG and HG p-values in cases where the p-value of one of the methods was smaller than 10^{-3} are shown. 51

S3 An example of the output of GOviz. A set of genes were ranked according to differential expression of 31 patients with CVD (cardio-vascular disease, either ischemic or non-ischemic) versus 6 patients with none failure hearts as reported in [7]. The enriched GO terms (mHG p-value $< 10^{-2}$ after bonfferoni correction for multiple GO term testing) and their parent GO terms up to the root are shown. The colors reflect the level of enrichment (yellow: 10^{-2} to 10^{-4}, orange: 10^{-4} to 10^{-6}, red: 10^{-6} to 10^{-8}) 53

S4 Observed versus expected length bias. For each of the 148 OC ChIP-chip experiments reported in [1] we ranked the yeast intergenic sequences according to their binding signal. The lengths of the top 300 sequences in each experiment were compared to the lengths of the rest of the sequences using a student t-test. The x axis is the t-test p-value and $y(x)$ is the number of TF experiments with $p \leq x$. The blue line is the observed cumulative distribution of the t-test p-values in the 148 experiments. The red line is the expected cumulative distribution of t-test p-values in randomly permuted sequence rankings. It can be seen that over half of the ChIP-chip experiments have a statistically significant difference between the lengths of sequences that bind the TF the strongest compared to the lengths of the rest of the sequences. 54

List of Tables

1 Examples of TFs for which DRIM identifies novel motifs.We further investigated these motifs and show evidence that indicate they are biologically functional. YPD, H_2O_2 and SM denote the ChIP-chip experimental conditions [1] in which the motifs were identified. 28

2 Enriched motifs associated with CpG methylation in 4 human cancer cell-lines and comparison to motifs in regions bound by the Polycomb complex. '# of experiments' corresponds to the number of replicate experiments of the same cell-line in which the same motif was independently identified. The CA repeat motifs have a variable length. 'Polycomb complex motif' denotes motifs that appear in regions bound by the Polycomb complex [8, 9, 10]. The motifs that are marked with a '*' have G-C content $> 66\%$. Their enrichments are partially attributed to the G-C content bias that is found in the CpG methylation data. 35

1 Abstract

Computational methods for discovery of sequence elements that are enriched in a target set compared to a background set are fundamental in molecular biology research. One example is the discovery of transcription factor binding motifs that are inferred from ChIP-chip (Chromatin Immuno-Precipitation on a microarray) measurements. Several major challenges in sequence motif discovery still require consideration: (i) the need for a principled approach to partitioning the data into target and background sets; (ii) the lack of rigorous models and of an exact p-value for measuring motif enrichment; (iii) the need for an appropriate framework for accounting for motif multiplicity; (iv) the tendency, in many of the existing methods, to report presumably significant motifs even when applied to randomly generated data. In this study we present a statistical framework for discovering enriched sequence elements in ranked lists that resolves the above four issues. Based on this framework we developed a software application, termed DRIM (Discovery of Rank Imbalanced Motifs), which identifies sequence motifs in lists of ranked DNA sequences.

We applied DRIM to ChIP-chip and CpG methylation data and obtained the following results: (i) Identification of 50 novel putative transcription factor (TF) binding sites in yeast ChIP-chip data. The biological function of some of them was further investigated and used in order to gain new insights on transcription regulation networks in yeast. For example, our discoveries enable the elucidation of the network of the TF ARO80.Another finding concerns a systematic TF binding enhancement to sequences containing CA repeats that suggests these repetitive elements play a mechanistic role in TF binding. (ii) Discovery of novel motifs in human cancer CpG methylation data. Remarkably, most of these motifs are similar to DNA sequence elements bound by the Polycomb complex that promotes histone methylation. Our findings thus support a model in which histone methylation and CpG methylation are mechanistically linked.

Overall, we demonstrate that our statistical framework embodied in the DRIM software tool is highly effective for identifying regulatory sequence elements in a variety of applications ranging from expression and ChIP-chip to CpG methylation data. DRIM is publicly available at: http://bioinfo.cs.technion.ac.il/drim.

2 Abbreviations

- TF, transcription factor;
- TFBS, transcription factor binding site;
- ChIP-chip, Chromatin Immuno-precipitation chip;
- mDIP, methyl-DNA immunoprecipitation;
- DRIM, discovery of rank imbalanced motifs;
- HG, Hyper-geometric;
- HGT, Hyper-geometric tail;
- mHG, minimal hyper-geometric;
- MM, Markov model.
- MOV, motif occurrence vector
- GO, gene ontology

3 Introduction

3.1 Background

This study examines the problem of discovering "interesting" sequence motifs in biological sequence data. A widely accepted and more formal definition of this task is:

Given a target set and a background set of sequences (or a background model), identify sequence motifs that are enriched in the target set compared to the background set.

The purpose of this study is to extend this formulation and make it more flexible so as to enable the determination of the target and background set in a data driven manner.

Discovery of sequences motifs or other attributes that are enriched in a target set compared to a background set (or model) has become increasingly useful in a wide range of applications in molecular biology research. For example, discovery of DNA sequence motifs that are over-abundant in a set of promoter regions of co-expressed genes (determined by clustering of expression data) can suggest an explanation for this co-expression. Another example is the discovery of DNA sequences that are enriched in a set of promoter regions to which a certain transcription factor (TF) binds strongly, inferred from ChIP-chip [11] measurements. Such enriched sequence motifs are promising TF binding sites (TFBS) candidates. The same principle may be extended to many other applications such as discovery of genomic elements enriched in a set of highly methylated CpG island sequences [6].

Due to its importance, this task of discovering enriched DNA subsequences and capturing their corresponding motif profile has gained much attention in the literature. Any approach to motif discovery must address several fundamental issues: defining a motif representation, choosing a background model, devising a score for capturing motif enrichment and devising a scheme for probing the motif space. We discuss these issues in the following subsections (Section 3.1.1 - 3.1.4).

3.1.1 Motif representations

The first key issue in motif discovery is to define "What exactly is a biological sequence motif?" and devise an appropriate computer model to capture it. Of course, different biological phenomena give rise to different types of motifs and may require different types of models. For example, TFBS motifs differ from splicing signal motifs in aspects such as motif length, variability, multiplicity and position in the genome.

There are several strategies for motif representation. The first uses a k-mer of symbols above $\{A,C,G,T\}$ to represent a motif. However, this model is over-simplistic and does not capture the stochasticity that often appears in real biological sequence motifs. An enhancement of this model is a k-mer above the 15 symbol

IUPAC alphabet $\{A$,C,G,T,R, Y, W, S, M, K, H, B, V, D, $N\}$ in which each letter represents a subset over $\{A, C, G, T\}$. For example S, which stands for Strong hydrogen bonds, is either G or C. More flexibility can be added by allowing mismatches or searching for motifs that are within a predefined Hamming distance. Examples of methods that use this type of representation include REDUCE [12], YMF [13, 14], ANN-SPEC [15] and a hyper geometric based method described in [16].

A different strategy for motif representation uses a PWM (Position Weight Matrix), which specifies the probability of observing each nucleotide at each motif position. Example of methods that use this representation are MEME [17], BioProspector [18], MotifBooster [19], DME-X [20] and AlignACE [21]. Both the k-mer and the PWM representations assume base position independence. Alternatively, higher order representations that capture positional dependencies have also been proposed (e.g. Bayesian networks motif representations [22, 23]). These representations circumvent the position independence assumption and enable the capturing of subtle correlations between binding site bases. However, they are also more vulnerable to over-fitting and lack of data for determining model parameters. The method described in this paper uses the k-mer model with symbols above IUPAC.

3.1.2 Background models

A sensible measure for a motif's enrichment should capture the difference between the number of motif occurrences in the target set of sequences compared to the number of occurrences in some background set or model. While the first task of enumerating/identifying the motifs in the target set is usually straightforward, the latter task depends on the nature of the background model. Strategies for devising the background can be classified into two main approaches: '*random sequence generation*' and '*random sequence selection*':

(i) The random sequence generation approach attempts to capture the notion of a 'typical' background sequence. Suppose we are given a set of sequences S and a target set of sequences T. Then it is possible to describe a 'typical' background sequence using a Markov Model (MM). A MM of order n is specified by the transition probabilities determined by the $(n+1)$-mer frequencies observed in S (or $S-T$). For example in [24] the authors used a MM of order $n=3$ to generate background sequences of promoter regions in yeast. This order of the MM enables the capturing of genomic patterns such as AAAA and TATA. A motif's enrichment was measured by comparing the actual number of motif occurrences in T to the expected motif occurrences in the sequences generated by the MM.

(ii) The random sequence selection approach compares the actual number of motif occurrences in the target set to the actual motif occurrence in the background set. One simple yet powerful hyper geometric method that is an embodiment of this strategy is described in [16]. In this study a motif's enrichment

was captured by computing the probability of the observed number of motif occurrences in T under the null hypothesis that the sequences in T were drawn from S at random.

One major advantage of the random sequence selection over the random sequence generation approach is that the first does not make any assumptions on the distribution of nucleotides. Such assumptions often fail to capture inherent complexities in genomic sequences and in turn lead to false motif predictions. For example, genomic patterns such as repetitive elements (e.g., CA or poly-A repeats) may be as long as 60 bases. However, constructing MMs of sufficient order to capture these events is unfeasible.

The framework described in our study uses the random sequence selection approach and is a natural extension of the approach of [16].

3.1.3 Motif enrichment scores

We turn to examine the question of how to devise a scoring scheme that captures motif enrichment. Many strategies for scoring motifs have been suggested in the literature. YMF [13, 14] and the work described in [24] associate each motif with a z-score that measures the number of standard divinations by which the total number of observed motifs in the target set exceed the expected number of motifs in a background set of sequences generated by a MM. The hyper-geometric approach of [16] uses the hyper-geometric tail as a measure for mtif enrichment. AlignACE [21] uses a Gibbs sampling algorithm for finding global sequence alignments and produces a MAP score. This score is an internal metric used to determine the significance of an alignment. MEME [17] uses an expectation maximization strategy and outputs the log-likelihood and relative entropy associated with each motif.

It is important to note that other then the work of [16], which produces an enrichment p-value, the other studies mentioned above produce a score that does not lend itself to such straight forward statistical interpretation. Instead, they use thresholds on their enrichment scores to determine what constitutes a significantly enriched motif or alternatively result to Monte-Carlo simulations on these scores to produce simulation based p-values.

3.1.4 Scanning the motif space

Once a motif score is devised most methods scan through a predefined motif space in search of significantly enriched motifs. Defining "What is the appropriate motif space?" is thus a fundamental issue. In some cases, the size of all biologically viable motifs can be restricted and the corresponding motif space size is amenable to exhaustive search. An example of such a case is described in [14] where TFBS motifs in the yeast genome, many of which have been shown to have a characteristics length of 6-10, are searched. However, other

instances such as TFBS of mammalians that have larger and fuzzier motifs lead to a practically infinite size of motif space (e.g. all 15^{20} motifs that reside in the space of 20-mers above the 15 symbol IUPAC alphabet), which cannot be scanned exhaustively in terms of running time. To deal with this some approaches use a heuristic search strategy (e.g., [17]). Other approaches scan part of the motif space exhaustively and generate motif seeds that are then further enlarged in a heuristic manner (e.g., [16]). Their underlying assumption is that large motifs are built from shorter motifs seeds that are sufficiently enriched to be detected. The study described herein makes this assumption as well.

Several excellent reviews narrate the different strategies for motif detection and use quantitative benchmarking to compare their performance [25, 26, 27, 28, 29]. A related aspect of motif discovery, which is outside the scope of this study, focuses on properties of clusters and modules of TF binding sites (TFBS). Examples of approaches that search for combinatorial patterns and modules underlying TF binding and gene expression include [30, 31, 32, 33, 34].

3.2 Open challenges in motif discovery

One issue of motif discovery that is often overlooked, concerns the partition of the input set of sequences into target and background sets. Many methods rely on the user to provide these two sets and search for motifs that are overabundant in the former set compared to the latter. However, the question of how to partition the data, i.e. set the boundary between the sets, is often unclear and the exact choice of sequences in each set arbitrary. For example, suppose that one wishes to identify motifs within promoter sequences that constitute putative TFBS. An obvious strategy would be to partition the set of promoter sequences into target and background sets according to the TF binding signal (as measured by ChIP-chip experiments). The two sets would contain the sequences to which the TF binds "strongly" and "weakly" respectively. A motif detection algorithm could then be applied to find motifs that are over-abundant in the target set compared to the background set. In this scenario the positioning of the cutoff between the strong and weak binding signal is somewhat arbitrary. Obviously, the final outcome of the motif identification process can be highly dependent on this choice of cutoff. A stringent cutoff will result in the exclusion of informative sequences from the target set while a promiscuous cutoff will cause inclusion of non-relevant sequences - both extremes hinder the accuracy of motif prediction. This example demonstrates a fundamental difficulty in partitioning most types of data. Several methods attempt to circumvent this hurdle. For example, REDUCE [12] uses a regression model on the entire set of sequences. However it is difficult to justify this model in the context of multiple motif occurrence (as explained below). In other work a variant of the Kolmogorov-Smirnov test was used for motif discovery [35]. This approach successfully circumvents arbitrary data partition. However it has other limitations such as the failure to address multiple motif occurrences in a single promoter, and

the lack of an exact characterization of the null distribution. Overall, the following four major challenges in motif discovery still require consideration:

(c1) The cutoff used in order to partition data into a target set and background set of sequences is often chosen arbitrarily.

(c2) Lack of an exact statistical score and p-value for motif enrichment. Current methods typically use arbitrarily-set thresholds or simulations, which are inherently limited in precision and costly in terms of running time.

(c3) A need for an appropriate framework that accounts for multiple motif occurrences in a single promoter. For example, how should one quantify the significance of a single motif occurrence in a promoter against two motif occurrences in a promoter? Linear models [12] assume that the weight of the latter is double that of the former. However, it is difficult to justify this approach since biological systems do not necessarily operate in such a linear fashion. Another issue related to motif multiplicity is low complexity or repetitive regions. These regions often contain multiple copies of degenerate motifs (e.g. ploy A repeats). Since the nucleotide frequency underlying these regions substantially deviates from the standard background frequency they often cause false motif discoveries. Consequently, most methods mask these regions in the preprocessing stage and thereby loose vital information that might reside therein.

(c4) Criticism has been made over the fact that motif discovery methods tend to report presumably significant motifs even when applied on randomly generated data [1]. These motifs are clear cases of false positives and should be avoided.

3.3 Data lends itself to ranking in a natural manner

In this paper we describe a novel method that attempts to solve the above mentioned four challenges in a principled manner. It exploits the following observation: Data often lends itself to ranking in a natural manner, e.g. ranking sequences according to TF binding signal; ranking according to CpG methylation signal; ranking according to distance in expression space from a set of co-expressed genes; ranking according to differential expression; etc. We exploit this inherent ranking property of biological data in order to circumvent the need for an arbitrary and difficult to justify data partition. Consequently, we propose the following formulation of the motif finding task:

Given a list of ranked sequences, identify motifs that are over-abundant at either end of the list.

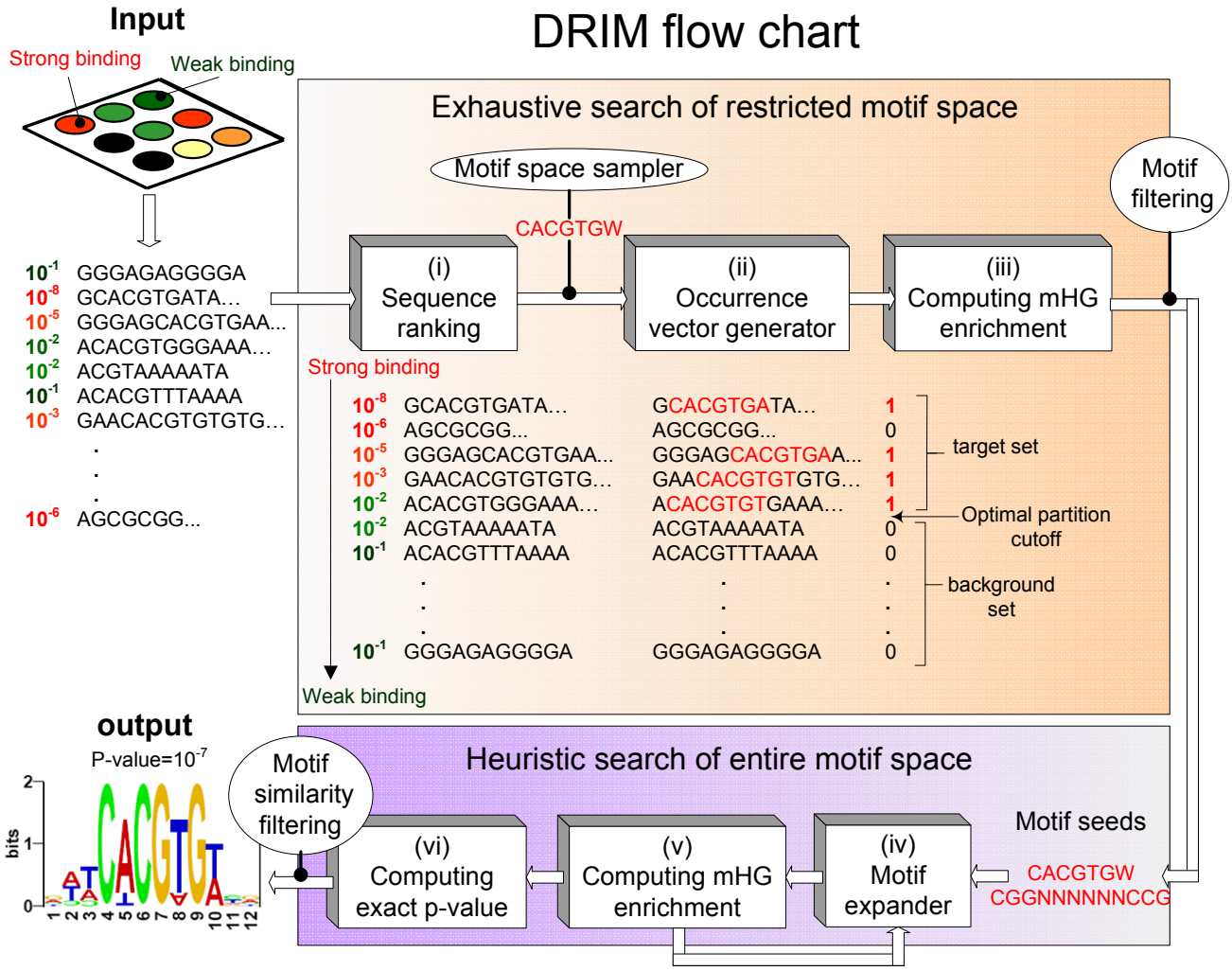

Figure 1: DRIM flow chart. DRIM receives a list of DNA sequences as input and a criterion by which the sequences should be ranked, for example TF binding signals as measured by ChIP-chip, and performs the following steps: (i) The sequences are ranked according to the criterion. (ii) A "blind search" is performed over all the motifs that reside in the restricted motif space (in this study the restricted motif space contains $\sim$ 100,000 motifs, see Section 4.5). For each motif an occurrence vector is generated. Each position in the vector is the number of motif occurrences in the corresponding sequence, (the figure shows the vector for the motif CACGTGW). (iii) The motif significance is computed using the mHG scheme, and the optimal partition into target and background sets in terms of motif enrichment is identified. The promising motif seeds are passed as input to the heuristic motif search model and the rest are filtered out. (iv,v) The motif seeds are expanded in an iterative manner, (the mHG is computed in each lap) until a local optimum motif is found. (vi) The exact mHG p-value of the motif is computed. If it has a p-value $< 10^{-3}$ then it is predicted as a true motif (the choice of this threshold is explained in Section 5.1). The output of the system is the motif representation above IUPAC, its PSSM, mHG p-value and optimal set partition cutoff.

Our solution employs a statistical score termed mHG (minimal Hyper Geometric) [36]. It is related with the concept of *rank-imbalanced motifs*, which are sequence motifs that tend to appear at either end of a ranked sequence list. In previous work [36], the authors used mHG in order to identify sequence motifs in expression data. We use this simple yet powerful approach as the starting point for our study.

3.4 Overview

The rest of this manuscript is divided into two main parts: in the Methods (Section 4) we develop the mHG probabilistic and algorithmic framework and explain how we deal with challenges (c1)-(c3) introduced in Section 3.2. In the Results (Section 5) we address challenge (c4) and describe novel biological findings that were obtained by applying our algorithms to biological data. Each part is self contained and can be read separately.

4 Materials and Methods

4.1 The minimum hyper-geometric (mHG) score

In this subsection we introduce the basics of the mHG statistics, and demonstrate how it can be applied in a straight forward manner to eliminate the need for an arbitrary choice of threshold. To explain the biological motivation of mHG consider the following scenario: suppose we have a set of promoter regions each associated with a measurement, e.g. a TF binding signal as measured by ChIP-chip [11]. We wish to determine whether a particular motif specified in IUPAC notation, say CASGTGW, is likely to be a TFBS motif. We rank the promoters according to their binding signals - strong binding at top of the list and the weak at the bottom (Figure 1i). Next, we generate a binary occurrence vector with 1 or 0 entries dependent on whether or not the respective promoter contains a copy of the motif (Figure 1ii). For simplicity we ignore cases where a promoter contains multiple copies of the motif, a restriction that will later be removed. Motifs that yield binary vectors with a high density of 1's at the top of the list are good candidates for being TFBS.

Let us assume for the moment that we know where to put a cutoff on the TF binding signal. The data could then be separated into 'strong binding promoters' (i.e. the target set) and 'weak binding promoters' (i.e. the background set). We are now interested in a particular motifs for which the target set contains significantly more occurrences than the background set. Let N be the total number of promoters, B of which contain the motif, and n the size of the target set. Let X be a random variable describing the number of motif occurrences in the target set. Assuming a uniform distribution over all occurrence vectors with these characteristics, X has a Hyper-Geometric (HG) distribution. Namely, the probability of finding *exactly* b occurrences in the target set is:

$$\text{Prob}(X = b) = \text{HG}(b; N, B, n) = \frac{\binom{n}{b}\binom{N-n}{B-b}}{\binom{N}{B}}. \tag{1}$$

The tail probability of finding b *or more* occurrences in the target set is:

$$\text{Prob}(X \geq b) = \text{HGT}(b; N, B, n) = \sum_{i=b}^{\min(n,B)} \frac{\binom{n}{i}\binom{N-n}{B-i}}{\binom{N}{B}}. \tag{2}$$

As we don't really know the target set and therefore do not know n nor b we employ a strategy that seeks a partition for which the motif enrichment is the most significant, and compute the enrichment under that particular partition. Formally, consider a set of ranked elements and some binary labeling of the set $\lambda = \lambda_1, ..., \lambda_N \in \{0, 1\}^N$. The binary labels represent the attribute (e.g. motif occurrence). The *minimum Hyper-*

Geometric (mHG) score is defined as:

$$\text{mHG}(\lambda) = \min_{1 \le n < N} \text{HGT}(b_n(\lambda); N, B, n), \tag{3}$$

where $b_n(\lambda) = \sum_{i=1}^{n} \lambda_i$. In conclusion, the mHG score reflects the surprise of seeing the observed density of 1's at the top of the list under the null assumption that all configurations of 1's in the vector are equiprobable. The cutoff between the top of the list and the rest of the list is chosen in a data driven manner so as to maximize the enrichment (Figure 1iii).

4.2 Calculating the p-value of the mHG score

The mHG flexible choice of cutoff introduces a multiple testing complication and therefore gives rise to the need of computing the exact p-value. In Section 7.1 we demonstrate several bounds for mHG p-value. These bounds may be used for rapid assessment of the p-value of a given mHG score, which can be instrumental in improving algorithmic efficiency. In this section we describe a novel dynamic programing algorithm for calculating the *exact* p-value of a given mHG score. This approach is related to a previously described approach for calculating exact p-values of other combinatorial scores ([37, 38], with details in [39]).

As noted in the previous section, the mHG score depends solely on the content of the label vector λ. Set W and B, and consider the space of all binary label vectors of size $N = W + B$ with B 1's and W 0's: $\Lambda = \{0,1\}^{(W,B)}$. Assume that we are given a vector $\lambda_0 \in \Lambda$, for which we calculate the mHG score $\text{mHG}(\lambda_0) = p$. We would like to determine $\text{pVal}(p) = \text{Prob}(\text{mHG}(\lambda) \le p)$ under a uniform distribution of vectors in Λ. Given an mHG score p we calculate $\text{pVal}(p)$ by means of path counting. The space of all label vectors $\Lambda = \{0,1\}^{(W,B)}$ is represented as a two-dimensional grid ranging from $(0,0)$ at the bottom-left to (W,B) at the top-right. Each specific label vector $\lambda \in \Lambda$ is represented by a path $(0,0) \rightarrow (W,B)$ composed of N distinct steps. The ith step in the path describing a vector λ is $(1,0)$ if $\lambda_i = 0$ and $(0,1)$ if $\lambda_i = 1$ (see Figure 2). Each point (w,b) on the grid corresponds to a threshold (on ranks) $n = w + b$, and the respective value $b = b_n(\lambda)$. It can therefore be associated with a specific HGT score: $\text{HGT}_n(\lambda) = \text{HGT}(b_n(\lambda); N, B, n)$. A subset of the points on the grid can be characterized as those points (w,b) for which $\text{HGT}(b; N, B, n) \le p$. We denote this subset $R = R(p)$ (see Figure 2).

The $(0,0) \rightarrow (W,B)$ path represents λ passing through N distinct grid points (excluding the point $(0,0)$), which correspond to N different HGT scores that are considered when calculating its mHG score: $\text{mHG}(\lambda) = \min_{1 \le n \le N} \text{HGT}_n(\lambda)$. $\text{mHG}(\lambda) \le p$ iff the path representing λ visits R. Denote by $\Pi(w,b)$ the total number of paths $(0,0) \rightarrow (w,b)$; by $\Pi_R(w,b)$ the number of paths $(0,0) \rightarrow (w,b)$ visiting R and by $\Pi_{\bar{R}}(w,b)$ the

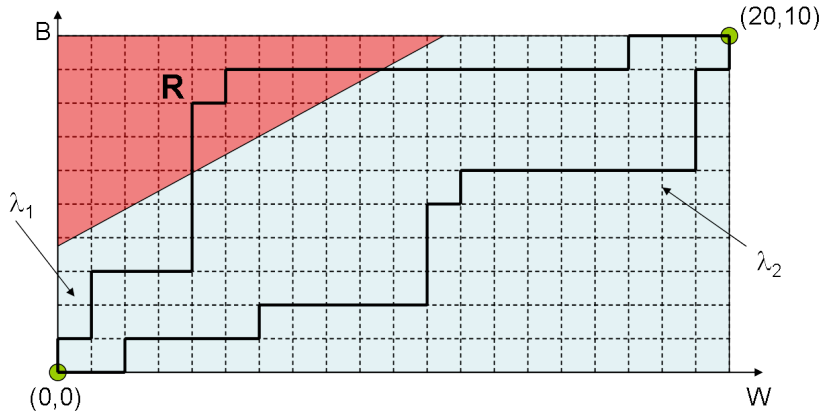

Figure 2: The two-dimensional grid used for calculating the mHG p-value. In this example $N = 30$, $B = 10$, $W = 20$ and $p = 0.1$. Light blue area describes all attainable values of w and b. Red area describes the subset R: all values of w and b for which $\text{HGT}(b; N, B, n) \leq p$, where $n = w + b$. Two $(0,0) \rightarrow (N,B)$ paths are depicted, representing the binary label vectors $\lambda_1 = \{1,0,1,1,0,0,0,1,1,1,1,1,0,1,0,0,0,0,0,0,0,0,0,0,0,0,1,0,0,0\}$ and $\lambda_2 = \{0,0,1,0,0,0,0,1,0,0,0,0,0,1,1,1,0,1,0,0,0,0,0,0,0,1,1,1,0,1\}$. The path λ_1 traverses R, demonstrating that $\text{mHG}(\lambda_1) \leq p$. The path λ_2 does not traverse R, demonstrating that $\text{mHG}(\lambda_2) > p$. The mHG p-value is calculated by counting all the paths from (0,0) to (W,B) that do not visit R divided by the total number of paths and subtracting this from 1.

number of paths $(0,0) \rightarrow (w,b)$ not visiting R. We then have:

$$\text{pVal}(p) = \frac{|\{\lambda \in \Lambda : \text{mHG}(\lambda) \leq p\}|}{|\Lambda|} = \frac{\Pi_R(W,B)}{\Pi(W,B)} = \frac{\Pi(W,B) - \Pi_{\bar{R}}(W,B)}{\Pi(W,B)} = 1 - \frac{\Pi_{\bar{R}}(W,B)}{\Pi(W,B)} \quad (4)$$

We calculate $\Pi_{\bar{R}}(w,b)$ by means of dynamic programming. Initially, set $\Pi_{\bar{R}}(0,0) = 1$, $\Pi_{\bar{R}}(-1,b) = 0$ for $0 \leq b \leq B$ and $\Pi_{\bar{R}}(w,-1) = 0$ for $0 \leq w \leq W$. Then, for each $0 \leq w \leq W$, and $0 \leq b \leq B$ calculate $\Pi_{\bar{R}}(w,b)$ using the formula:

- 0, if $(w,b) \in R$
- $\Pi_{\bar{R}}(w,b) = \Pi_{\bar{R}}(w-1,b) + \Pi_{\bar{R}}(w,b-1)$, if $(w,b) \notin R$

In summary, to compute the p-value $\text{pVal}(p)$ of an mHG score p we first calculate $\Pi_{\bar{R}}(W,B)$. Trivially, we have $\Pi(W,B) = \binom{W+B}{B}$ and $\text{pVal}(p)$ may be directly computed from (4). The time complexity of the algorithm is $O(W \cdot B)$, which is also $O(N^2)$ obviously.

4.3 Multi-dimensional mHG Score

So far we have dealt with enrichment of binary attributes, in which a 1 or 0 indicated whether or not the attribute appeared. There are cases where one would like to associate a number with an attribute. We revisit our example from section 4.1 in which we tried to determine whether a particular motif is likely to be a TFBS motif. The promoters were ranked according to their binding signals and the corresponding binary

occurrence vector was generated. Notice, that some promoters may contain several copies of a particular motif. Clearly, this information is valuable, as it may affect TF binding potential, and should be incorporated in the enrichment analysis. However, how exactly to incorporate this information is not obvious. For example, consider two motif occurrence vectors generated for two different motifs. The top 10 entries of the vectors are all 1's and 2's respectively. Is the second motif more enriched than the first? Obviously, this depends on how rare 2 motif occurrences are compared to 1 in the corresponding vectors. If the frequency of 2's is lower than that of 1's then the second motif is more significant. However, if they are equally frequent (this is often the case for degenerate motifs such as poly A's) then both motifs are equally enriched.

To quantitatively capture this notion and address motif multiplicity in a data driven manner, we propose a multi-dimensional hyper geometric model, which extends the previously-defined framework for enrichment analysis to non-binary label vectors. We define the multi-dimensional hypergeometric score (multiHG) for a set S of size N consisting of $k+1$ subsets $S_0, S_1, S_2...S_k$ of respective sizes $N-(B_1+B_2+...B_k), B_1, B_2...B_k$. Given a subset $S' \subset S$ of size n, the probability of finding exactly b_1 elements of S_1 and b_2 elements of S_2... b_k elements of S_k within S' is:

$$multiHG(N, B_1, ..., B_k, n, b_1, ..., b_k) = \frac{\binom{n}{b_1, ..., b_k}\binom{N-n}{B_1-b_1, ...B_k-b_k}}{\binom{N}{B_1, ..., B_k}} \tag{5}$$

Let $X_1, ..., X_k$ be random variables describing the number of 1's,...,k's respectively at the top n positions of λ. The multi hyper - geometric tail probability (multiHGT) of seeing at least b_1 1's, at least b_2 2's,...and at leaset b_k k's at the top n positions of the vector is:

$$multiHGT(N, B_1, ..., B_k, n, b_1, ..., b_k) = P(X_1 \geq b_1, ..., X_k \geq b_k) = \sum_{i=b_1}^{\min(B_1,n)} ... \sum_{i=b_k}^{\min(B_k, n-\sum_{j=1}^{k-1} i_j)} \frac{\binom{n}{i_1, ..., i_k}\binom{N-n}{B_1-i_1, ...B_k-i_k}}{\binom{N}{B_1, ..., B_k}} \tag{6}$$

The definition of the mHG score can now be extended to multi-dimensional vectors. Formally, let λ be a uniformly drawn label vector $\lambda=\lambda_1,...,\lambda_N \in \{0...k\}^N$ containing B_1 1's, B_2 2's... B_k k's and $N - \sum_{j=1}^{k} B_j$ 0's. We would like to test for enrichment of 1's, 2's...k's at the top of λ by computing the minimum multi-HGTs

over all prefixes of λ:

$$multi - mHG(\lambda) = \min_{1 \le n \le N} (multiHGT(N, B_1, ..., B_k, n, b_1(n, \lambda), ..., b_k(n, \lambda)), \tag{7}$$

where b_j(n,λ) = $\sum_{i=1}^{n} I(\lambda_i = j)$. The exact p-value of the multi-dimensional mHG can be computed using a path enumeration strategy, similar to the one described in section 4.2, in a k dimensional space. The details on how to compute this p-value in a 3-dimensional space are explained in Section 4.3.1.

For the sake of brevity, in the rest of the manuscript, we use the HG and $multi - HG$ notations interchangeably when the correct interpretation can be understood from the context.

4.3.1 P-value of the multi-dimensional mHG score

In section 4.2 we explained how to compute the exact mHG p-value of binary vectors by means of path counting. Here we demonstrate how to extend the idea to multi-dimensional mHG p-values. Consider a 3-dimensional case for which we have fixed values of W, B, Y and $N = W + B + Y$. The p-value of a given 3-dimensional mHG$^{(3)}$ score p is calculated using a 3-dimensional grid ranging from $(0, 0, 0)$ to (W, B, Y). A specific trinary label vector $\lambda \in \{0, 1, 2\}^N$ is represented by a path $(0, 0, 0) \rightarrow (W, B, Y)$ where the i^{th} step in the path is $(1, 0, 0)$ if $\lambda_i = 0$, $(0, 1, 0)$ if $\lambda_i = 1$ or $(0, 0, 1)$ if $\lambda_i = 2$. Each point (w, b, y) on the grid corresponds to a rank $n = w + b + y$ and the respective values $b_n = b(n, \lambda)$ and $y_n = y(n, \lambda)$. Consequentially each point (w, b, y) on the grid can also be associated with a specific HGT$^{(3)}$ score: HGT$^{(3)}_n(\lambda)$ = HGT$(b_n, y_n; N, B, Y, n)$.

As in the binary case, we define R to be the subset of the points on the grid for which HGT$^{(3)}_n(\lambda) \le p$. We then count the number of paths $(0, 0, 0) \rightarrow (W, B, Y)$ not traversing R by dynamic programming, denoted $\Pi_{\bar{R}}(W, B, Y)$. The mHG$^{(3)}$ p-value is:

$$\text{pVal}(p) = 1 - \frac{\Pi_{\bar{R}}(W, B, Y)}{\binom{N}{B,Y}} \tag{8}$$

This can be computed in $O(W \cdot B \cdot Y)$. The idea is summarized in Figure 3.

4.4 Partition-limited mHG score

Recall, from Section 4.1, that mHG is as the minimum HGT score calculated over all partitions that agree with the given ranking. In many cases it is reasonable to consider HGT scores obtained only at a subset of all possible partitions, either due to some external information, or for algorithmic efficiency. Three possible

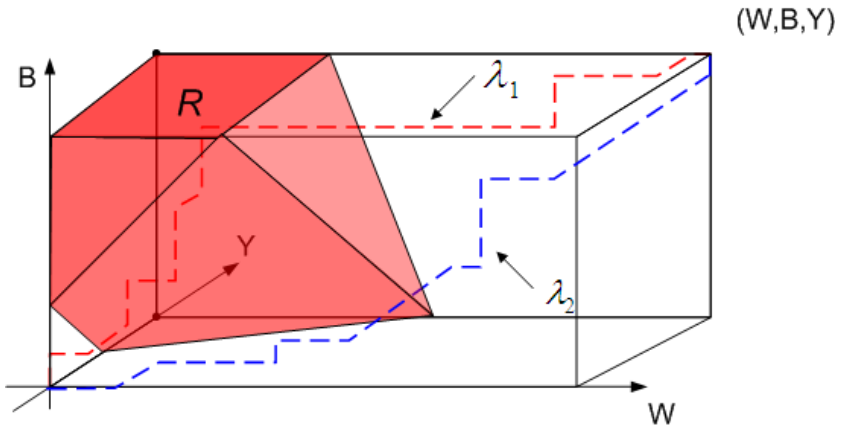

Figure 3: The 3-dimensional grid used for calculating the 3-dimensional mHG p-value. Given W, B, Y and p one can compute the region R (red region in the figure): the subset of all points (w,b,y) in the grid for which $\text{HGT}(b, y; N, B, n) \leq p$, where $n = w + b + y$ and $N = W + B + Y$. Two $(0, 0, 0) \rightarrow (W, B, Y)$ paths are depicted. The path λ_1 traverses R, demonstrating that $\text{mHG}(\lambda_1) \leq p$. The path λ_2 does not traverse R, demonstrating that $\text{mHG}(\lambda_2) > p$. The mHG p-value is calculated by counting all the paths from (0,0,0) to (W,B,Y) that do not visit R divided by the total number of paths, and subtracting this from 1.

partition-limited variations are:

- Consider only the first $n_{\max}$ partitions. This is useful when we are interested mainly in enrichment that occurs only for thresholds in a fixed top of the ranked list, and not at elsewhere.
- Consider only every n_{step}th partition. This is useful for improving algorithmic efficiency and tightening bounds, at the expense of the accuracy of the mHG score.
- In some cases one may be interested in computing HGT scores of sets that contain elements from both the top and the bottom of a ranked list. For example, some TFs such as Rap1, may bind to promoters and cause either over or under expression. In such cases one is interested in searching for motifs that reside in a target set containing the promoters of the over and under expressed genes. Instead of using two fixed thresholds on the expression signal, one for determining over-expression and the other for under-expression, we consider all sets containing the top n and the bottom m sequences. For a given motif, we compute the minimal HG score over all these pairs of thresholds.

For the first two variations, it is possible to devise respective variations for the calculation of the bounds and accurate p-value that were described in Section 4.2, for example see Figure 4.

4.5 The DRIM Software

We implemented a software tool called DRIM (*Discovery of Rank Imbalanced Motifs*), which uses the mHG framework for measuring motif significance. We now turn to describe the principle algorithmic issues as well as biological considerations used in the design and implementation of of DRIM.

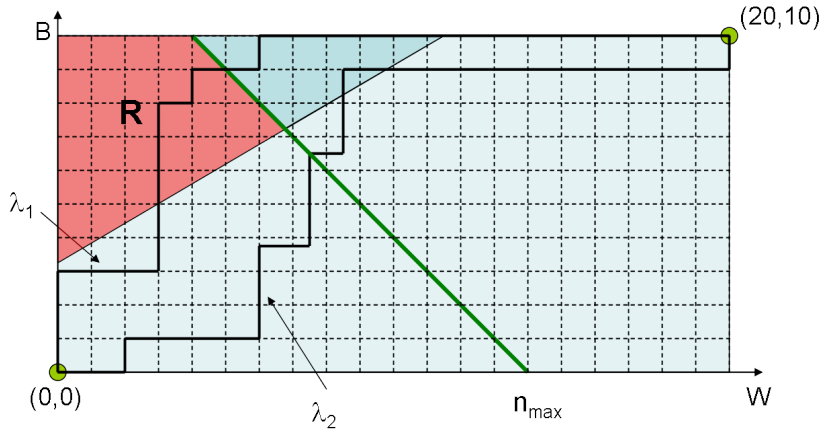

Figure 4: The two-dimensional grid used for calculating the partition limited mHG p-value. In this example $N = 30$, $B = 10$, $W = 20$, $p = 0.1$ and $n_{max} = 14$. The red area describes the subset R: all values of w and b for which $\text{HGT}(b; N, B, n) \leq p$, and $n = w + b \leq n_{max}$. The light blue area describes all attainable values of w and b. The partition limited mHG p-value is calculated by counting all the paths from (0,0) to (W,B) that do not visit R divided by the total number of paths, and subtracting this from 1.

4.5.1 Work-flow

The following subsection describes DRIM's work-flow. A summary of the DRIM work-flow is also captured in Figure 1. The application is based on the mHG statistical framework. DRIM receives a list of ranked DNA sequences as input (for example sequences ranked according to TF binding signals) and returns the enriched sequence motifs, their confidence, and the threshold in which maximal enrichment was detected.

Exhaustive search of the restricted motif space: Ideally we would like to exhaustively search through the space of all biologically viable motifs and identify those that are significantly enriched at the top of the ranked list. However, this is infeasible in terms of running time (for example the space of viable TF binding sites includes motifs of size up to 20, i.e. 15^{20} k-mers). We therefore resolve to a simple strategy where the motif search is broken into two stages: first an exhaustive search on a restricted motif space is performed. The 'motif seeds' that are identified in the preliminary search are used as a starting points for a heuristic search of larger motifs in the entire motif space. The restricted motif space S is the union of two subspaces S_1 and S_2: $S_1 = \{A, C, G, T, R, W, Y, S, N\}^7$ where the IUPAC degenerate symbols (i.e. R, Y, W, S, N) are restricted to a maximum of 2 and $S_2 = \{A, C, G, T\}^3 N^{3-25} \{A, C, G, T\}^3$. The rational behind the usage of the restricted IUPAC alphabet in S_1 instead of the complete 15 symbol alphabet stems from DNA - TF physical interaction properties and TFBS data-base statistics as explained in previous work [24]. S_2 captures motifs that contain a fixed gap (different motifs can have different gap sizes), which is characteristic of some TFs such as Zinc fingers.

mHG enrichment: For each of the motifs in S we generate a ranked occurrence vector and compute the enrichment in terms of the multi-dimensional mHG. Due to running time considerations we restrict the multi dimensional mHG to 3 dimensions. This means that the model assumes each intergenic-region contains either 0, 1 or $\geq$2 copies of a motif. To test whether this assumption is reasonable in the case of true TFBS motifs we examined the occurrence distribution of TFBS motifs that were experimentally verified in S. cerevisiae, see Figure 5. It can be seen that the assumption holds for the 5 TFs that were tested since the majority of all intergenic regions contained either 0, 1 or 2 copies of the TFBSs. At the end of this stage only motif seeds with mHG score $< 10^{-3}$ are kept (choice of threshold is explained in section 5.1). Similar motifs are filtered (as explained in Section 4.5.5) and the remaining motif seeds are fed into the heuristic search module for expansion, Figure 1iii-iv.

Motif expansion by heuristic search: The filtered motif seeds are used as starting points for identification of larger motifs that do not reside in the restricted motif space. This is done through an iterative heuristic process that employs simulated annealing. The objective function is to minimize the motif mHG p-value. We tested two different strategies for determining valid moves in the motif space. In the first, we define a move from motif M1 to M2 as valid if M1 and M2 are within a predefined Hamming distance D. All valid moves are equiprobable. Additional bases can also be added to the motif flanks thus enabling motif expansion. Note that the mHG adaptive cutoff is recalculated at each step. In the second strategy all the motif occurrences in the target set that are within hamming distance D are aligned. A consensus motif above IUPAC is extracted and the algorithm attempts to move to that motif. While the second strategy converges much faster than the first it is also more prone to local minimum (in the final application we use the second strategy with D = 1). At the end of the process the exact p-value of each of the expanded motifs is computed. To correct for multiple motif testing the p-value is then multiplied by the motif space size. Only motifs with corrected p-value $< 10^{-3}$ are reported.

Running time: The DRIM application has been implemented in C++. The "blind search" imposes that over $\sim 100,000$ motifs are checked for enrichment in each run. It is therefore paramount to optimize the above procedures in order to enable a feasible running time. There are two bottlenecks in terms of running time: the motif occurrence vector generation and the mHG computation. We developed several optimization schemes to improve both (for details see Section 4.5.2 - 4.5.4). For example, running time on a list of 6000 sequences with an average size of 480 bases is $\sim$3 minutes on a Pentium IV, 2 GHz, (a 3000 fold improvement over the naive implementation (with out the optimizations) that took $\sim$9000 minutes per single run).

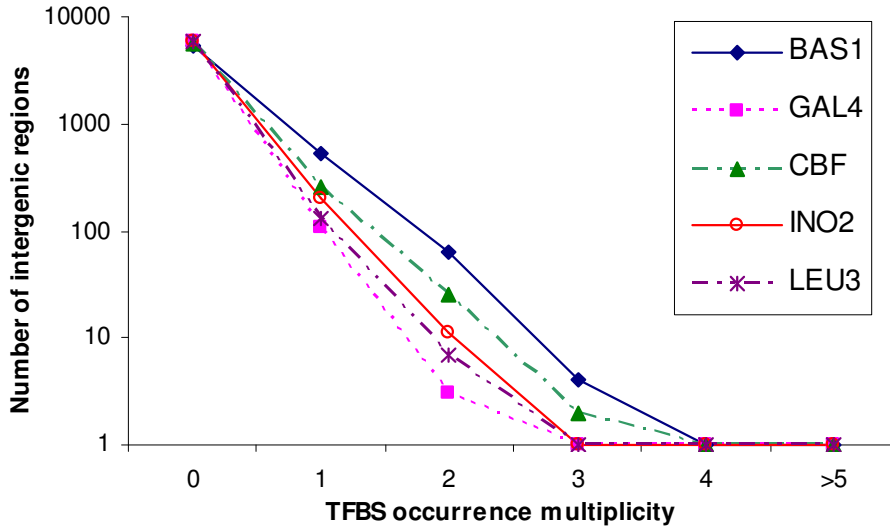

Figure 5: The distribution of TFBS occurrence multiplicities per intergenic region in Saccharomyces cerevisiae is shown for five TFs whose TFBS motif was experimentally verified. Note that the y-axis is logarithmic and that the fraction of sequences with 3 or more occurrences is less than 0.1%.

4.5.2 How to compute the mHG score efficiently

Computing mHG in O(N · B) : Let N be the the size of a binary vector λ; B is the total number of 1's in λ; b is the number of 1's in $\lambda_1, ..., \lambda_n$. A naive approach for computing the HG score at a fixed n takes $O(N)$ (see Equation 1). Consequentially, computing HGT takes $O(N \cdot B)$ (see Equation 2). The mHG score of λ can be computed by simply "sliding down" the vector and computing the HGT scores at each of the N ranks yielding a time complexity of $O(N^2 \cdot B)$. This strategy is inefficient in terms of running time, especially in the context of motif finding where the mHG score is computed many times - for each motif in the motif space. Another issue involves numerical errors that may arise in the computation of HG for large N's. To solve these issues some applications use the binomial distribution in order to approximate the HG distribution [40].

We propose a strategy that circumvents the need for such approximations. Furthermore, we show how to compute the HG and HGT scores in $O(1)$ and $O(B)$ respectively thus reducing the mHG computation to $O(N \cdot B)$. The idea is to slide down the vector and compute the HG score at position $n+1$ using the already known HG score at the previous position, n (see equations 9-11), as follows

The recursion base is:

$$HG(n=0, b=0, N, B) = \frac{\binom{0}{0}\binom{N}{B}}{\binom{N}{B}} = 1, \tag{9}$$

If entry n+1 in the vector is '0' then the HG score can be computed as follows:

$$HG(n+1,b,B,N) = HG(n,b,B,N) \cdot \frac{(n+1)(N-n-B+b)}{(n+1-b)(N-n)}, \tag{10}$$

If entry n+1 in the vector is '1' then the HG score can be computed as follows:

$$HG(n+1,b+1,B,N) = HG(n,b,B,N) \cdot \frac{(n+1)(B-b)}{(b+1)(N-n)}, \tag{11}$$

While the above recursive formulas were developed for binary vectors, the same principle can be expanded to vectors over higher dimensions. The recursive formulas for trinary vectors, as used by the DRIM application, are given in Section 7.2.

Computing mHG in O(N + B^2) : Another optimization of the mHG score computation takes advantage of the following observation:

Theorem 4.1

$$n < m \Rightarrow \textit{HGT}(b;N,B,n) \leq \textit{HGT}(b;N,B,m) \tag{12}$$

Proof: Let $\Lambda = \{0,1\}^N$ be the space of binary vectors with B 1's and $N-B$ 0's. b_i is the number of 1's at the top i positions of a vector $\lambda \in \Lambda$ and $\lambda(i) \in \{0,1\}$ is the value of the i^{th} element of the vector. For any $n < m$:

$$\text{HGT}(b;N,B,n) = \frac{|\{\lambda | b_n(\lambda) \geq b\}|}{|\Lambda|} \leq \frac{|\bigcup_{i=n}^{m}\{\lambda | b_i(\lambda) \geq b\}|}{|\Lambda|} = \frac{|\{\lambda | b_m(\lambda) \geq b\}|}{|\Lambda|} = \text{HGT}(b;N,B,m). \tag{13}$$

This property can be used in order to improve the efficiency of the mHG score computation, especially when $N >> B$. The idea is to compute the mHG only over partitions n_i ($1 \leq i \leq B$) for which $\lambda(n_i) = 1$ instead of minimizing over all possible N partitions (as in Equation 3). The above property guarantees that the minimal HGT over these B partitions is equal to the minimal HGT score over all N partitions. This point is illustrated in Figure 6. Since the computation of HGT is bounded by $O(B)$ we can now compute the mHG score in $O(N+B^2)$. In practice, the mHG computation can be further improved by using the partition limited mHG variation explained in Section 4.4.

4.5.3 How to compute the mHG p-value efficiently

Devising the algorithm for computing the mHG p-value (Section 4.2) in terms of path counting is conceptually convenient. However, such a strategy may become impractical in terms of computer precision for large

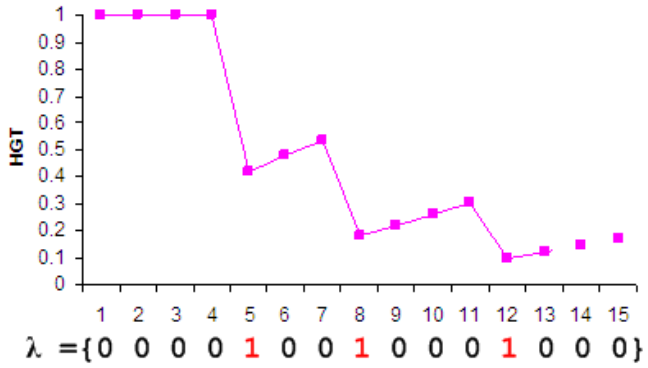

Figure 6: HGT scores over all possible 15 partitions of a given vector $\lambda = (0,0,0,0,1,0,0,1,0,0,0,1,0,0,0)$. The local minima HGT scores are achieved in partitions n=5,8,12 where $\lambda(5) = \lambda(8) = \lambda(12) = 1$.

vectors. For example, Equation 4 for computing the mHG p-value of a vector of size N=10,000 with B=1000 1's requires the computation of $\binom{10,000}{1000}$, which is beyond machine precision. We introduce a modification of the p-value computation algorithm, which yields the same theoretical results but in practice avoids such numerical problems.

Consider an urn with N balls, B of which are black and W white. The probability of drawing w white and b black balls in n draws ($n = w + b$) can be computed using the following recursive formulation:

$$P(w,b) = P((w,b)|(w-1,b)) \cdot P(w-1,b) + P((w,b)|(w,b-1)) \cdot P(w,b-1) \tag{14}$$

where $P((w,b)|(w-1,b)) = (W-w+1)/(B+W-b-w+1)$ is the probability of drawing a white ball on the n^{th} turn taken that w-1 white balls and b black balls have been drawn until the n-1 turn. Similarly $P((w,b)|(w,b-1)) = (B-b+1))/(B+W-b-w+1)$. We also define $P(0,0) = 1$, $P(-1,b) = 1$ and $P(w,-1) = 0$.

Recall the space of all label vectors $\Lambda = \{0,1\}^{(W,B)}$ represented by a two dimensional grid ranging from (0,0) at the bottom-left to (W,B) at the top-right (as described in Section 4.2). Each path from (0,0) to (W,B) corresponds to a specific vector $\lambda \in \Lambda$. For each point (w,b) on the grid we can associate $P(w,b)$ (defined in Equation 14), which is the probability of observing w 0's and b 1's at the top n positions of a uniformly drawn vector from Λ. As in Section 4.2 we can also associate a HGT score, $HGT(b;N,B,n)$, with each point on the grid and define a subset of points R(p) such that each point in R(p) has $HGT(b;N,B,n) \leq p$. Trivially, $P(W,B) = 1$, which means that the probability of randomly drawing a vector λ with W 0's and B 1's at the top N positions of the vector is equal to 1. What we are interested in is identifying $P(W,B)$ under the constraint that non of the vector prefixes $0 \leq n \leq N$ visit R(p). To do this we add the following constraint to Equation 14: $P(w,b) = 0$ if $(w,b) \in R(p)$. The mHG p-value is equal to $P(W,B)$.

Using the recursive formula in Equation 14 and a dynamic programming procedure the p-value can be computed in O($W \cdot B$). We note that the same principle is used for computing the multi-dimensional p-value.

4.5.4 Optimizing the occurrence vector generation

A straight forward strategy for generating the motif occurrence vector (MOV) is to exhaustively scan all sequences and identify the number of motif occurrences in each sequence. Denote the total length of all sequences N, and the size of the motif space M, than this strategy for constructing a MOV is bound by $O(MN)$. In practice M and N may be as large as large (M = $\sim 10^5$, N = $\sim 10^7$). Performing a motif search on one ranked list takes approximately 9000 minutes on a Pentium IV, 2 GHz. Performing multiple runs (as done in this study) becomes infeasible in terms of running time. To overcome this we exploit the fact that the same set of sequences is often used in different experiments. As a preprocessing step we construct a lookup table that maps motif prefixes of size m with their locations in the sequences. Given such a table, constructing a MOV of a motif of size m' (where $m' \geq m$) can be done by searching for motif occurrences only at locations where the corresponding motif prefix appears. The approximate running time improvement (assuming equiprobable nucleotide distribution) is $(1/4)^m$. In practice we use $m = 7$. This idea was further expanded to deal with motifs that contain IUPAC symbols.

4.5.5 Measuring motif similarity

Devising a motif similarity measure is important in order to enable a quantitative comparison between our predicted motifs to those reported in other studies. This measure is also useful for filtering similar motifs as performed by DRIM. First, we define a similarity measure between IUPAC symbols. Let α and β be symbols over the IUPAC alphabet - $\alpha, \beta \in \{A, C, G, T, R, Y, W, S, M, K, H, B, V, D, N\}$. Each IUPAC symbol can also be represented by a specific subset over $\{A, C, G, T\}$. We define a distance between α and β as follows:

$$\delta(\alpha, \beta) = 1 - 2\frac{|\alpha \cap \beta|}{|\alpha| + |\beta|}. \tag{15}$$

Notice that this metric maintains the following properties:

1. For identical symbols $\delta(\alpha, \beta) = 0$ (i.e. identical symbols have a distance of 0) ;
2. For disjoint symbols $\delta(\alpha, \beta) = 1$ (e.g. $\{A\}$ vs. $\{C\}$ or $W = \{A, T\}$ vs. $S = \{C, G\}$) ;
3. $0 \leq \delta(\alpha, \beta) \leq 1$ (e.g. α=$\{A, C, G\}$, β=$\{A, G\} \rightarrow \delta(\alpha, \beta) = 0.2$) .

We define the distance between two motifs a and b above IUPAC with sizes m and n as follows:

$$D(a,b) = \sum_{i=1}^{\min(n,m)} \delta(a_i, b_i) + w_1 u, \tag{16}$$

where u is the number of unpaired bases and w_1 is the weight assigned to such occurrences. It is sometimes useful to allow shifts in the motif comparison. For example, $D(ACGTAC, CGTACG)$ = 6, indicating that the two motifs are non-similar. However, a more careful examination reveals that the two motifs share a common substring containing 5 bases. To capture this type of similarity in the motif comparison we consider all $n + m - 1$ possible shifts when aligning the motifs (no gaps are permitted in the alignment) and choose the one that minimizes the distance. When comparing our predicted motifs to those reported in the literature as well as when filtering similar motifs produced by our method we use w_1 = 0.6. Two motifs are considered similar if:

$$\frac{D(a,b)}{mean(|a|,|b|)} \leq 0.5. \tag{17}$$

The exhaustive search module produces a list of significant motifs seeds, many of which are highly similar and overlapping. The similarity measure is used to filter similar motifs and generate a list of unique motifs. To this end we apply the following simple procedure:

(i) Rank the motifs according to their enrichment

(i) Take out the most significant motif in the list and store it in the list of unique motifs

(ii) Erase all the motifs that are similar to it

(iii) Repeat this process until list is empty.

The unique motifs are used as input to the heuristic module.

4.6 Characteristics of data sets

4.6.1 ChIP-chip dataset

A number of assays have been recently developed that use immunopercipitation based enrichment of cellular DNA for the purpose of identifying binding or other chemical events and the genomic locations at which they occur. Location analysis, also known as ChIP-chip (Chromatin Immuno-Precipitation chip), is a technique that enables the mapping of transcription binding events to genomic locations at which they occur [11, 41]. The process is summarized in Figure 7. In the first step of this technique a cell population under study is treated with formaldehyde to cross-link transcription factors to DNA they are bound to. A sonicated

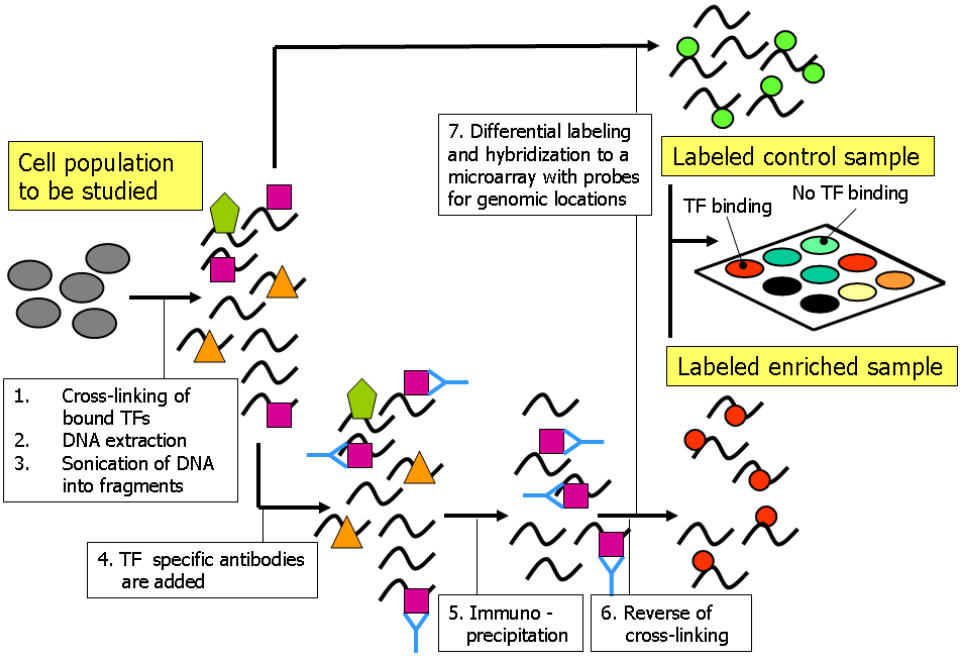

Figure 7: A summary of the location analysis (ChIP - chip) procedure

DNA extract from that cell population is then separated into two samples. For one (the control sample), no action is taken. For the other (the enriched sample) an antibody is used to bind to a transcription factor of interest. Using chromatin immunoprecipitation (ChIP) results in retaining only the DNA sequences bound to the TF which is bound to the antibody. After reverse cross linking we have two mixtures of DNA - one enriched for sequences to which the TF is bound and one that is representative of the total DNA of the original cell population. These are differentially labeled using fluorescence dyes and the mixture is hybridized to a microarray representing genomic regions of interest. The output of the assay is a fluorescence dye ratio at each spot of the array. If spots are taken to represent genomic regions then we can regard the ratio and p-value associated with each spot as an indication of TF binding in the corresponding region.

We applied DRIM to the S. cerevisiae genome-wide location data reported in Harbison et al. [1] and Lee et al. [42]. The first consists of the genomic occupancy of 203 putative TFs in rich media conditions (YPD). In addition, the genomic occupancy of 84 of these TFs was measured in at least one other condition (OC). In each of the experiment the genomic sequences were ranked according to the TF binding p-value. Surprisngly, we observed that 69 of the 203 ranked sequence lists of YPD had significantly longer sequences at the top of the list (first 300 sequences) compared to the rest of the list with t-test p-value $\leq 10^{-3}$. We observed a similar phenomenon in 76 of the 148 ranked sequence lists of OC experiments (see Figure 8 and Figure S4). In other words, for some TFs, *longer sequences are biased toward stronger binding signals*.

This observation is unexpected since, although longer probes hybridize more labeled material than shorter probes the increase should be proportional in both channels. This type of length bias may cause spurious results under our model assumptions and hence the final dataset, termed 'Harbison filtered dataset', refers to the remaining 207 experiments (135 YPD, and 72 OC) of 162 unique TFs that did not have length bias (Supplementary Table S1).

An additional ChIP-chip data set was constructed using the data reported in Lee et al. [42] containing 113 experiments in rich media. The data is partially exclusive to the data of Harbison et al. [1]. The same filtering procedure was performed, resulting in a set of 65 experiments, termed 'Lee filtered dataset'.

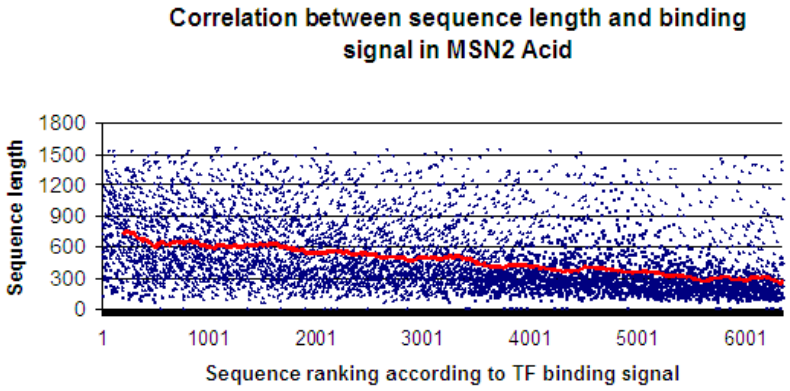

Figure 8: Sequence length bias observed in ChIP-chip data of the TF MSN2 measured in an acidic condition. The yeast intergenic regions were ranked according to their binding to MSN2, (strong to weak binding appear from left to right). The figure shows the sequence lengths at each rank. The red trend line (a moving average of 200) indicates that sequences that are ranked higher in terms of TF binding are also longer. A student t-test comparing the lengths of the top 300 versus the rest of the sequences yielded a highly significant p-value $\leq 10^{-40}$.

4.6.2 Methylated CpG dataset

Using a technique similar to ChIP-chip, termed methyl-DNA immunoprecipitation (mDIP), enables the measurement of methylated CpG island patterns [43, 6]. The third dataset contains the CpG island methylation patterns of 4 different human cancer cell-lines (Caco-2, Polyp, Carcinoma, PC3) where several replicate experiments were done for each of the cell-lines. In each of these experiments the CpG methylation signal was measured in $\sim$ 13,000 gene promoters as reported in [6].

5 Results

5.1 Proof of principle

We begin by testing our method on synthetically generated clear-cut positive and negative control cases. We do this in order to verify that DRIM accurately identifies motifs in well characterized and experimentally verified examples and at the same time avoids false identification of motifs in randomly ordered genomic sequences. The latter objective is of particular importance since the issue of false identification has been mentioned as one of the main shortcomings of motif discovery approaches. For example, in a previous study six different motif discovery applications were used to search for TFBS motifs [1]. Each of the programs attempted to measure the significance of its results using one or more enrichment scores. The authors report that the applications outputted high-scoring motifs even when applied to random selections of intergenic regions. In another work the authors generated clusters of genes whose expression patterns correlate to the expression of a particular TF [44]. These clusters were then analyzed for enriched motifs. Again, the authors report that random sets, with sizes matching those of the real clusters, contained a large number of motifs with significant scores.

To test our method's false prediction rate we performed the following negative control experiment: 5 different random permutations of ChIP-chip data were generated by randomly selecting 400 promoters and randomly permuting their ranks. DRIM was then applied to these sets and scanned over $\sim$100,000 different motifs in each set. None of the motifs that were scanned had a significant corrected mHG p-value $< 10^{-3}$. Note that in order to get the corrected p-values two levels of multiple test corrections are performed: correcting for the number motifs that are tested and correcting for multiple cutoffs that are tested as part of the mHG optimization process. In section 5.5 we describe a comparison to other methods using the same random set benchmarking.

How do the p-values of random motifs compare to those of true biological motifs? To test this we chose 5 TFs (BAS1, GAL4, CBF1, INO2 and LEU3) whose motif binding sites are well characterized and experimentally verified. We applied DRIM to the ChIP-chip data of these TFs as reported in [1]. In all instances the true motifs were identified with corrected p-values of 10^{-6}, 10^{-9}, 10^{-76}, 10^{-18}, 10^{-8} respectively. A comparison of the p-value distribution of the motifs in the randomly ordered sequences with that of the verified TFBS motifs is given in Figure 9. In all instances the true TFBS motifs were predicted with p-values that were several orders of magnitude more significant than the best p-value of a motif in the randomly permuted data. This indicates that the enrichment signals of true TFBS, as captured by the mHG p-value, are clearly distinct from the signals we expect to find in random rankings of genomic sequences.

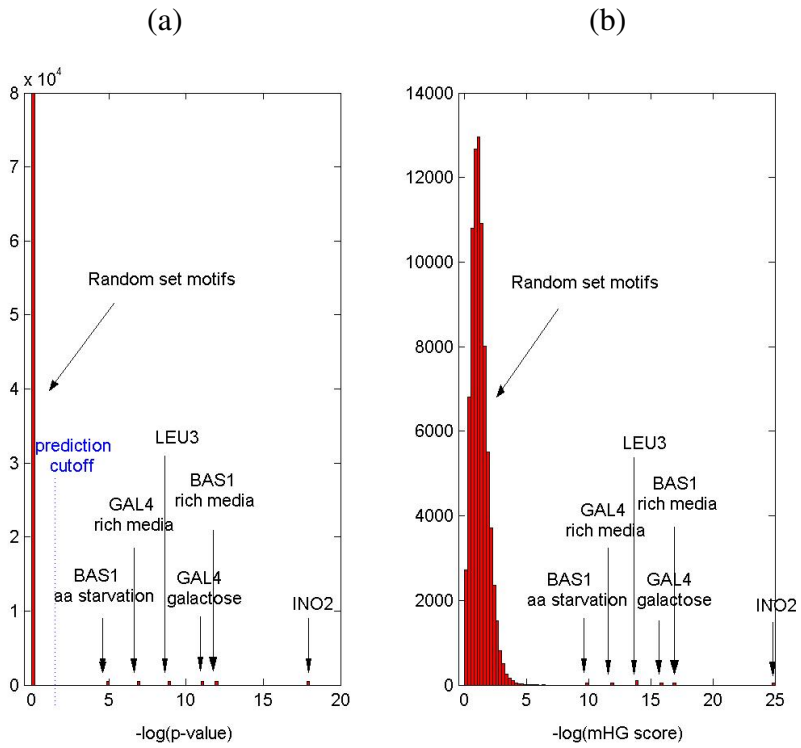

Figure 9: Comparison of mHG score and p-value distributions for motifs in randomly ranked sequences with those of true TFBS motifs in ranked lists derived from the corresponding ChIP-chip assays. $\sim$100,000 motifs were scanned in 400 randomly ranked genomic sequences, and their corresponding corrected p-value (a) and mHG score (b) were recorded. The corrected p-values involves two levels of multiple test corrections: correction on the number of motifs that were tested and correction for the multiple cutoffs that are tested as part of the mHG optimization process. None of the tested motifs had a corrected p-value$<10^{-3}$. DRIM was applied on the ChIP-chip data of 5 TFs and the mHG scores and corrected p-values of the true TFBS motifs (as previously determined experimentally) were recorded. In all instances the true TFBS motifs were predicted with p-values that were several orders of magnitude more significant than the best random set motif p-value.

5.2 TFBS prediction in yeast using ChIP-chip data

To further test the effectiveness of our method we used it for identification of TFBS in yeast by applying it to the Harbison and Lee filtered ChIP-chip datasets, (for details regarding datasets see Section 4.6). In each of the ChIP-chip experiments the intergenic-regions were ranked according the TF binding signal (we use the p-value of enrichment for the sequence represented on the array). This was given as input to DRIM, which then searched for motifs that tend to appear densely at the top of the ranked lists. If such a motif does exist, with a p-value less than 10^{-3}, then we hypothesize that it is biologically significant and that it contributes to the TF's binding, either directly or indirectly.

The results on the 207 experiments in the Harbision filtered dataset are given in Supplementary Table S2. A TF was assigned a motif if such was found in at least one condition. We compared the DRIM predictions with previously reported TFBS discoveries in ChIP-chip that incorporated predictions of 6 other motif discovery methods and conservation data [1]. The comparison is summarized in Figure 10.

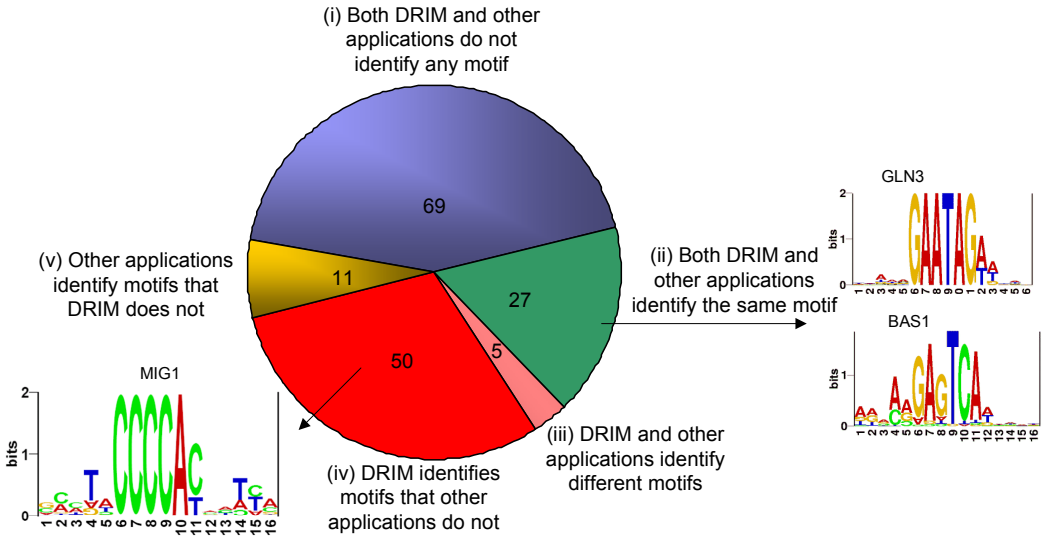

Figure 10: Comparison between predictions of DRIM and published predictions of 6 other methods and conservation data as reported in [1]. Overall, out of 162 unique TFs, DRIM identified significant motifs for 82 TFs with p-value$<10^{-3}$. Out of the 162 TFs, DRIM and the other applications agree on 96 TFs: 27 TFs for which a similar motif was found and 69 TFs for which no significant motifs were found. There are 5 TFs for which the motifs predicted by DRIM and other applications differ; 11 for which the other applications identified motifs that DRIM did not and 50 for which DRIM identified a motif that the other applications did not (for details see Supplementary Table S2 and Table S3). Sequence logos were generated using the *RNA Structure Logo* software [2].

Overall, DRIM identified 50 motifs that were not picked up by the 6 other methods as reported in [1]. We further investigated these putative TFBS for additional evidence that they are biologically meaningful. First, we found that 7 of them (ASH1, GCR1, HAP2, MET31, MIG1, RIM101 and RTG3) are in agreement with previously published results that are based on experimental techniques other then ChIP-chip. Second, we compared them to a list of conserved regulatory sites in yeast that was recently inferred using conservation based algorithms [45]. 10 of our putative TFBS match these conserved sites (ARG81, ARO80, ASH1, CRZ1, DAL81, HAP2, IME1, MET31, MIG1 and RTG3). Taken together, these findings provide a strong indication that at least some of the new motifs identified by DRIM are true biological signals. In the following subsections (5.2.1-5.2.3) we focus on a few of these putative TFBS (see Table 1) and present additional evidence that supports their biological role. We use these findings to discover new interactions in the yeast genetic regulatory network.

5.2.1 Aro80 transcription regulatory network

The Aro80 TF regulates the utilization of secondary nitrogen sources such as aromatic amino acids, as part of the Ehrlich pathway [46]. In particular it is involved in the regulation of 2-phenylethanol, a compound with a rose-like odor, which is the most used fragrance in the perfume and cosmetics industry [47]. Due to

TF	Motif	p-value	Note
Aro80 (YPD and SM)	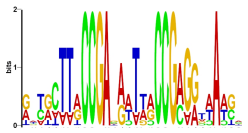	10^{-11}	For details see Section 5.2.1
ARR1 (YPD), GCR2 (YPD), IME4 (YPD), ACE2 (YPD), AFT2 (H_2O_2), MAL33 (H_2O_2), SFP1(H_2O_2)	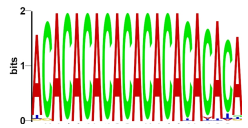	10^{-6}, 10^{-5}, 10^{-19}, 10^{-8}, 10^{-21}, 10^{-27}, 10^{-4}	For details see Section 5.2.2
IME1 (H_2O_2)	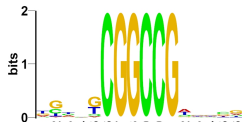	10^{-6}	For details see Section 5.2.3
Met4 (YPD and SM), Met31 (YPD), Met32 (YPD and SM)		10^{-5}, 10^{-4}, 10^{-8}	For details see Section 5.2.3
Met4 (YPD and SM), Met31 (YPD), Met32 (YPD and SM)	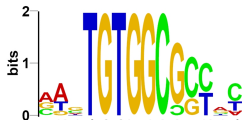	10^{-3}, 10^{-3}, 10^{-3}	For details see Section 5.2.3

Table 1: Examples of TFs for which DRIM identifies novel motifs.We further investigated these motifs and show evidence that indicate they are biologically functional. YPD, H_2O_2 and SM denote the ChIP-chip experimental conditions [1] in which the motifs were identified.

its commercial potential, the optimized production of this substance has received much attention [47].

We identified the remarkably large motif, WWNCCGANRNWNNCCGNRRNNW, in Aro80 rich media ChIP-chip data [1] with p-value $< 10^{-11}$ (see Figure 1). We refer to this putative binding site as BS_{Aro80} . Furthermore, we discovered the same motif in two other independent sources of data: Aro80 rich media experiment in the Lee filtered dataset and Aro80 SM condition (amino acid starvation), both with p-value$<$ 10^{-6}. Only 7 copies of this motif occurred in the entire yeast genome. These 7 copies are distributed among 4 promoters, 3 of which have 2 copies of BS_{Aro80} each. This unusual motif distribution is combinatorially surprising and therefore suggests biological significance. We note that BS_{Aro80} shares some similarity with a previously reported Aro80 motif [3, 45]. However, the sequence of BS_{Aro80} provides new insights to the mechanism of the yeast Ehrlich pathway that cannot be explained by the previously described motif:

(i) It was previously shown that Aro80 enhances the transcription of Aro9 and Aro10 [3, 46]. We found BS_{Aro80} in the promoters of both genes - two copies in each promoter.

(ii) Interestingly, BS_{Aro80} appears in the promoter of the gene coding to the Aro80 protein. Since the

BS_{Aro80} motif appears only in 4 promoters in the entire genome it is highly unlikely that this occurred by chance. We therefore hypothesize that Aro80 self-regulates its own transcription by directly binding to its own promoter.

(iii) The fourth promoter (when ranking according to Aro80 rich media ChIP-chip data [1]) contains two BS_{Aro80} elements, one on the sense and the other on the anti-sense. This configuration is shared by two divergently transcribed genes, NAF1 and Esbp6. The latter gene was previously shown to have increased transcription in the presence of phenylalanine as sole nitrogen source [46], suggesting it may play a role in the Ehrlich pathway. Esbp6 is a monocarboxylate permease and might be involved in the transfer of substrates of the Ehrlich pathway across the plasma membrane

(iv) We analyzed the conservation of BS_{Aro80} in 4 yeast strains and found all 7 of its copies to be conserved in the different strains.

(v) Aro80 belongs to the Zn_2Cys_6 family of TFs that are known to bind CCG elements separated by a spacing. Indeed, in addition to other conserved nucleotides the motif contains CCG gapped tri-nucleotides.

(vi) In a previous study, in order to identify cis-acting sequences involved in Aro9 induction, a series of deletions were produced in the Aro9 promoter region and the expression of a reporter gene was monitored [3]. The authors concluded that the sequence $\text{CCGN}^7\text{CCGN}^7\text{CCGN}^7\text{CCG}$ in the Aro9 promoter is responsible for Aro80 binding. We note, however, that the changes in expression caused by the mutations can be interpreted differently and in fact they are even more consistent with our BS_{Aro80} motif. Deletions or mutations that simultaneously altered all motif copies in the promoter dramatically reduced expression, while those which altered only some of the copies caused a more mild decrease. Other deletions that did not affect any BS_{Aro80} motif did not affect the expression at all. A detailed analysis of the BS_{Aro80} element in respect to these mutagenesis studies is given in Figure 12.

A putative transcription network of Aro80 that incorporates these findings is shown in Figure 11a. Another interesting observation is that adjacent to the BS_{Aro80} motif there are three GATA binding sites (see Figure 11b). We used these findings (and other information) to further hypothesize on the mechanism by which the Aro80 pathway is regulated (for details see Section 7.4).

The predicted motif BS_{Aro80} exemplifies the usefulness of the mHG flexible cutoff. Our process partitioned the data into a target set containing the top first 4 promoters (the only promoters in the genome in which the motif resides) and a background set containing the rest of the promoters. Other methods that used a fixed binding signal cutoff (p-value$< 10^{-3}$) for partitioning the data included 16 other promoters in the

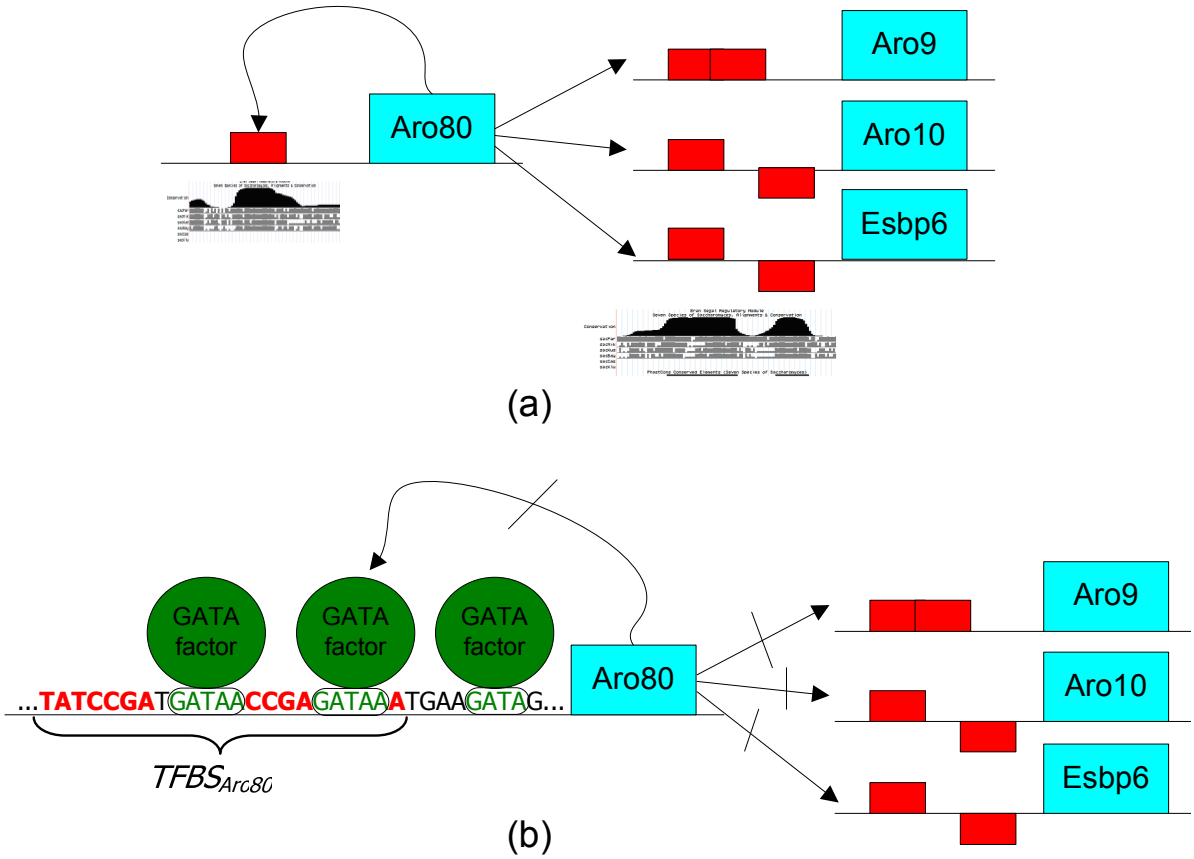

Figure 11: The hypothetical regulatory network of Aro80. Copies of the BS_{Aro80} motif (on the sense and anti sense) are shown as rectangles on the promoter regions. (a) BS_{Aro80} is conserved in 4 strains of yeast as shown using the UCSC browser conservation plots. Aro80 regulates the utilization of secondary nitrogen sources such as aromatic amino acids by binding genes that participate in the catabolism of aromatic amino acids. We hypothesize that it also binds to its own promoter region and introduces a positive feedback self loop. (b) Part of the Aro80 promoter sequence is shown with bases of the BS_{Aro80} motif colored in red. Interestingly, there are three GATA binding sites that are adjacent to the BS_{Aro80} motif (bases colored in green). These sites bind GATA factors that are known to play a role in nitrogen catabolite repression. We hypothesize that they are also involved in the repression of Aro80 expression by physically binding to the region near BS_{Aro80} thus making it inaccessible to Aro80 binding. This in turn breaks the positive feedback loop and represses the expression of Aro80 itself and other Aro80 regulated genes.

target set, in addition to the 4 promoters in which BS_{Aro80} appears. Consequentially the signal to noise ratio decreases, which might explain why other methods did not identify the BS_{Aro80} element.

Taken together, our results suggest the predicted BS_{Aro80} motif is indeed a Aro80 binding site.

5.2.2 CA repeats are correlated with TF binding

We identified a bi-nucleotide CA repeat motif with a variable length ranging from 6 to 62, in the Harbision filtered dataset. The CA repeat motif was found to be highly enriched for seven TFs: ARR1, GCR2, IME4

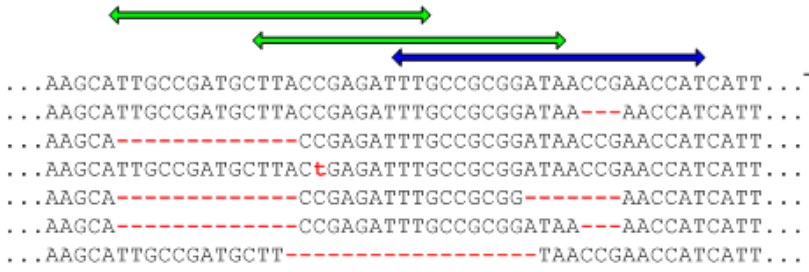

Expression of reporter Gene	Number of intact motif copies
7440	3
6890	2
4890	1
1465	1
370	0
248	0
4	0

Figure 12: Compatibility between the BS_{Aro80} motif identified by DRIM and previously reported mutagenesis studies [3]. The Aro9 promoter region from base -169 to -133 as well as 6 other copies containing mutations and deletions are shown. These regions were used in order to construct hybrid promoters and measure the expression of a reporter gene, which is dependent on the binding of Aro80 to the promoter[3]. The two partially overlapping copies of BS_{Aro80} that reside in the Aro9 promoter and an additional sequence element that is similar to the canonic BS_{Aro80} (2 different bases) are marked with green and blue arrows respectively. It can be seen that the expression values can be explained in terms of intact BS_{Aro80} copies, i.e more intact copies yield higher expression.

and ACE2 in rich media condition and AFT2, MAL33, SFP1 in H_2O_2Hi condition. Furthermore, for two of these TFs (GCR2, IME4), we rediscovered the same CA repeat motif in the Lee filtered dataset. This means that for certain TFs there is a highly significant correlation between a sequence's capacity to bind the TF and the presence of a CA repeat in the sequence. A visual example of the CA repeat occurrences in the yeast genome and their correlation with TF binding is presented in Figure 13. This type of low complexity motifs are often filtered by current methods (see Section 3.2 for details). One exception is a recent work in which a CACACACACAC sequence was found to be enriched in Rap1 experiments [48]. It has been previously hypothesized that CA repeats might have a functional role in TF binding [49]. It was proposed that CA repeats, which are often conserved in evolutionary distant organisms, are likely to impose a unique DNA structure that aids in the identification of other specific regulatory elements [49]. Our findings constitute concrete evidence to this phenomena in 7 (of 82) different TFs. They are also in agreement with another work in which the sequences in the human gamma-globin gene promoter required for efficient transcription were identified using in vitro site-directed mutagenesis [50]. These sequences included a CA repeat subsequence. Taken together, our findings and other observations suggest CA repeats may play a role in the DNA binding of some TFs.

5.2.3 Detection of indirect TF-DNA binding using ChIP-chip

IME1 is a TF which activates transcription of early meiotic genes. We identified a novel motif, CGGCCG, with p-value $<10^{-11}$ that is enriched in the sequences to which IME1 binds in H_2O_2 condition experiments. We note that this motif is a perfect palindrome, which is often indicative of a true binding site. IME1 interacts with Ume6, also a transcriptional regulator of early meiotic genes, that was previously shown to bind the same

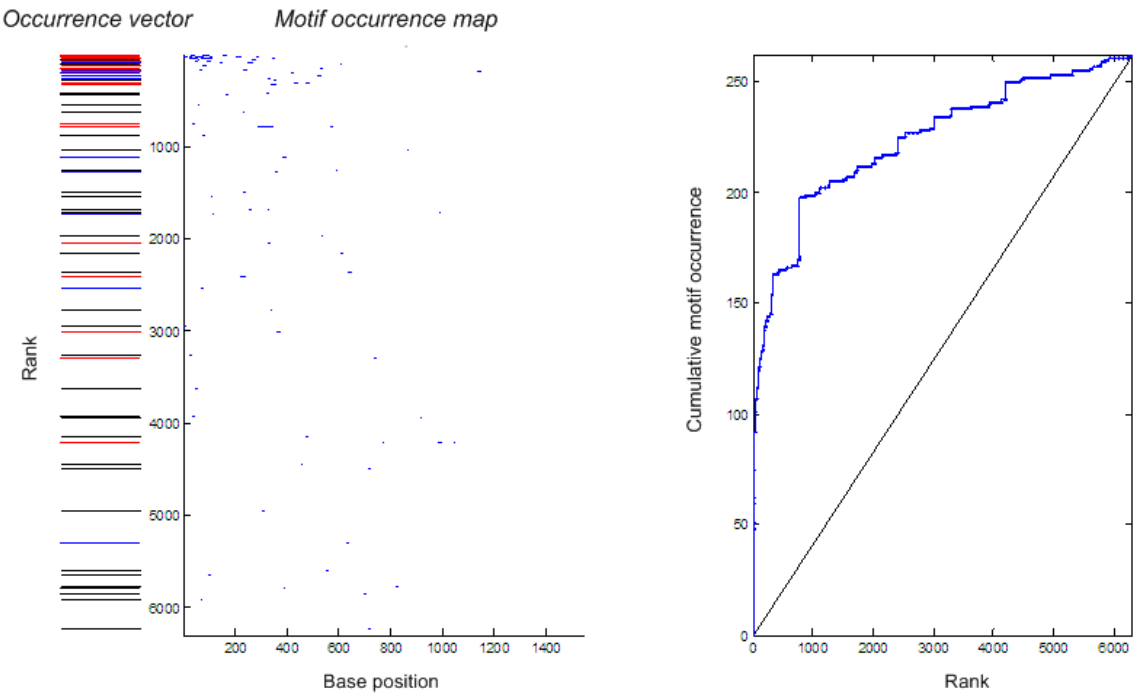

Figure 13: Visualization of CA repeat occurrences in the yeast genome and their correlation with TF binding. ∼6000 intergenic regions were ranked according to their binding to the TF AFT2 in a H_2O_2Hi ChIP-chip experiment [1] and the motif CACACACA was searched in each of the regions. On the left is the motif *occurrence vector* with white, black, blue and red lines indicating whether the corresponding region contains 0, 1, 2 or >2 motif occurrences respectively. It can be seen that the top of the vector is significantly more dense than the rest of the vector indicating that the CA repeats are highly correlated with AFT2 binding. In the center is the *motif occurrence map* in which the blue lines mark the bases of the motif occurrences. It can be seen that that the density of motif occurrences increases in regions that are ranked high in the list . On the right is a plot of the expected vs. observed cumulative motif occurrences. The x-axis represents the ranked intergenic regions and the y-axis is the cumulative motif occurrence as function of rank. The height of the y-axis is the total number of motif occurrences.

DNA motif, CGGCCG [51]. It is therefore likely that the IME1 motif we discovered is due to the following scenario: IME1 binds to Ume6, which binds to CGGCCG sequences on the DNA. The cross linking in the ChIP-chip protocol fixes these bindings and the immuno-precipitation of IME1, actually precipitates the entire complex. We therefore get an enriched CGGCCG sequences in IME1 experiments due to indirect binding to this DNA motif.

In another example, we identified the same two distinct motifs, M_1=TGTGGCSS and M_2=CACGTG, in rich media ChIP-chip experiments of three different TFs: Met4, Met31 and Met32. Furthermore, we re-discovered the same motifs in other experimental conditions of the same TFs. Met4, Met31 and Met32 are three factors involved in the sulfur amino acid pathway, and the fact that the same two motifs were independently predicted for each of the TFs is unlikely to occur by chance, indicating the predictions are biologically meaningful. In a previous work it was shown that Met4 is tethered to the DNA sequence AAACTGTG via two alternative complexes Met4-Met28-Met31 and Met4-Met28-Met32 (the binding is thought to occur via Met31/32) [4]. This sequence partially overlaps motif M_1. Furthermore, the complex Met4-Met28-Cbf1 was

shown to bind motif M_2 [5]. Previous findings are summarized in Figure 14a. The above explains why we predict M_1 for Met4 and M_2 for Met31/32. However, it does not explain why we also predict M_2 for Met4 and M_1 for Met31/32. The most likely explanation for this is the existence of a direct interaction between the two complexes Met4-Met28-Cbf1 and Met4-Met28-Met31/32. If such an interaction exists then the cross-linking would fix the two complexes and cause the immuno-precipitation of either Met4, Met31 and Met32 to precipitate the same set of sequences thus causing the same motifs to appear in the experiments of all 3 TFs, which is exactly what DRIM identifies. This point is illustrated in Figure 14b. The idea of direct interaction between the two complexes is also in agreement with a previous work [4].

Overall the results shown in this subsection demonstrate that DRIM is able to pick up on previously ignored subtle signals in ChIP-chip data that stem from *indirect* bindings of factors to DNA. This type of information can be useful for inferring novel protein-protein interactions.

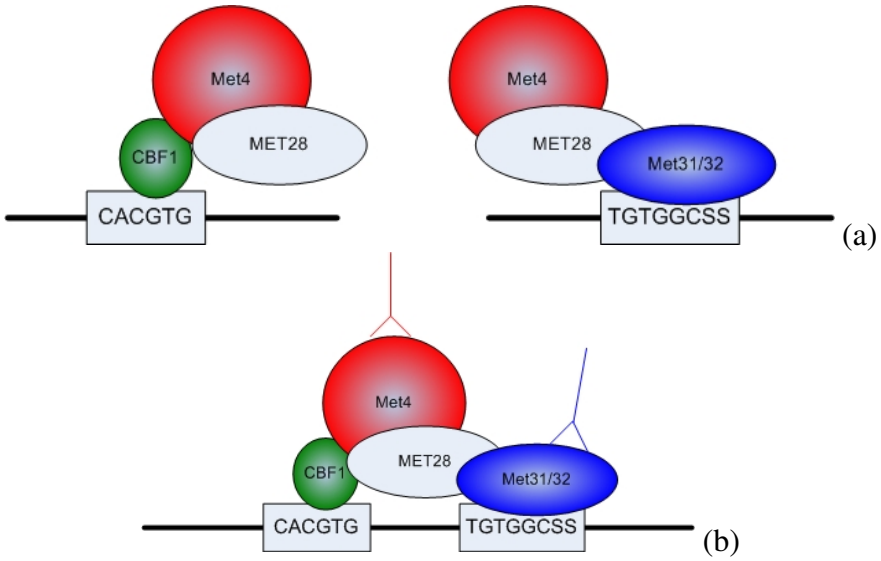

Figure 14: (a) Schematic representation of Met4-Met28-CBF and Met4-Met28-Met31/32 complexes [4, 5]. (b) A hypothetical Met4-Met28-CBF-Met31/32 complex. Immuno-precipitation of any of the TFs in the complex will precipitate the same set of sequences, which explains why DRIM identifies the same two motifs for all TFs in the complex.

5.2.4 Condition dependent motifs

A comparison was made between the predicted motifs of the same TF in different experimental conditions (see Table S2). These seem to fall into two main categories: (i) motifs whose enrichment is condition dependent and (ii) motifs whose enrichment is condition invariant, suggesting the TF is bound to the DNA regardless of condition. In the latter, although the same motif was predicted in different conditions the motif enrichment varied considerably. For instance, the GAL4 binding site CGGN^{11}CCG, previously reported in [11] and other literature, was predicted in both YPD and galactose conditions. However, the enrichment

varied considerably with p-values 10^{-7} and 10^{-11}, respectively. This several fold difference in enrichment is consistent with what is known about the role of GAL4 in galactose metabolism. It suggests that GAL4 has a preference to bind CGGN^{11}CCG DNA regardless of condition. However, in the presence of galactose and absence of glucose, this preference becomes much more significant. Another example of a condition invariant motif whose binding strength is subject to experimental condition is that of Aro80, see section 5.2.1.

This demonstrates that DRIM can be used not only to identify binding sites but also to distinguish between different modes of TF binding.

5.3 Motif discovery in Human methylated CpG islands

We turn to examine our method's ability to predict sequence motifs that stem from data other than TF binding. To this end, DRIM was applied to the dataset containing the human cancer cell-line methylated CpG islands (for dataset details see Section 4.6.2) in order to try and identify motifs that are enriched in hyper methylated regions. The promoters were ranked according to their methylation signal, hyper-methylated promoters at the top. Note that different replicates of the same cell-line may yield different ranking of the promoters.

DRIM identified significantly enriched motifs in each of the 4 cancer cell-lines. Table 2 shows all the motifs that were independently discovered in at least 2 different replicates of the same experiment or are in agreement with previous work [6]. Overall, DRIM discovered 13 motifs: 10 novel motifs and 3 that have been previously predicted in hyper methylated CpG island promoters in the same cancer cell-lines [6]. Some of these motifs have also been independently identified in methyled CpG regions of other cell-lines [52, 53].

Remarkably, 9 of the novel 10 motifs have been identified in DNA regions to which the proteins of the Polycomb complex bind [8, 9, 54]. The Polycomb complex is involved in gene repression through epigenetic silencing and chromatin remodeling, a process that involves histone methylation. The fact that these two distinct key epigenetic repression systems, namely histone methylation and CpG methylation, bind to regions that share a similar set of sequence motifs suggests they are linked. To further establish this link we applied DRIM to Polycomb complex bound promoters in human embriyonic fibroblasts [10]. We found 4 motifs that are similar to the CpG methylation motifs (Table 2). Our findings are consistent with a recent paper that showed that the EZH2 protein binds methyltransferases via the a Polycomb complex [55].

We note that most of the motifs we found are similar across more than one type of cancer-cells, e.g. variants of the GCTGCT motif appear in both Caco-2, PC3 and Polyp1. This suggests that the same DNA binding factors are involved in CpG methylation of different types of cancer-cells. It is also important to note that some of the motifs we discovered are G-C rich. The enrichment of these motifs may be partially attributed to the G-C content bias that is found in the CpG methylation data. Interestingly, some of the motifs we found to be correlated with CpG methylation are low complexity motifs such as the CA repeat and GA

repeats. A visual example of this correlation is given in Figure 15

The DRIM motif identification process can be used not only to identify novel motifs but also to partition the data in a biologically meaningful manner. In [6] the authors used a fixed threshold on the methylation signal (p-value < 0.001) in order to partition the dataset. Consequently they identified 135 hyper-methylated promoters. A more data driven partition would be to use the threshold that yielded the maximal motif enrichment. For example in the Caco2 cell-line, we identified the same motif as in the previous work [6]. However the motif maximal enrichment was found in the top 209 promoters (an increase of 54% in target set size).

Cell-line	**CpG methylation Motif**	**# of experiments**	**Average p-value**	**Notes**	**Polycomb complex motif**
Caco-2	SSCCCCANG*	4	$< 10^{-10}$	Novel prediction	Yes [8, 10]
Caco-2	CNGCTGC*	3	$< 10^{-5}$	Novel prediction	Yes [8]
Caco-2	GAGGGA	2	$< 10^{-4}$	In agreement with [6]	
Caco-2	DGAGAGV	2	$< 10^{-4}$	Novel prediction	Yes [8, 54, 10]
Carcinoma	CA repeat	2	$< 10^{-79}$	Novel prediction	Yes [8, 9]
PC3	CA repeat	1	$< 10^{-7}$	Novel prediction	Yes [8, 9]
PC3	GGGGTNCC*	1	$< 10^{-6}$	In agreement with [6]	Yes [10]
PC3	ACACNCAC	2	$< 10^{-10}$	In agreement with [6]	
PC3	GCTGC	2	$< 10^{-5}$	Novel prediction	Yes [8]
PC3	RGCGCAA	2	$< 10^{-4}$	Novel prediction	
Polyp1	CA repeat	2	$< 10^{-58}$	Novel prediction	Yes [8, 9]
Polyp1	CNNGCGCC*	3	$< 10^{-13}$	Novel prediction	Yes [10]
Polyp1	GCTGCNBB	2	$< 10^{-6}$	Novel prediction	Yes [8]

Table 2: Enriched motifs associated with CpG methylation in 4 human cancer cell-lines and comparison to motifs in regions bound by the Polycomb complex. '# of experiments' corresponds to the number of replicate experiments of the same cell-line in which the same motif was independently identified. The CA repeat motifs have a variable length. 'Polycomb complex motif' denotes motifs that appear in regions bound by the Polycomb complex [8, 9, 10]. The motifs that are marked with a '*' have G-C content $> 66\%$. Their enrichments are partially attributed to the G-C content bias that is found in the CpG methylation data.

5.4 Motif discovery in Human ChIP-chip data

Human TFBS tend to be longer and "fuzzier" than TFBS of lower eukaryotes and it is important to evaluate our method's performance on such motifs. To this end we applied DRIM to the ChIP-chip experiments of HNF1α, HNF4α, HNF6 in liver and pancreas islets [56] as well as to that of CREB [57]. For each of the TFs we generated a list of sequences containing 1000 bases upstream and 300 downstream the transcription start site (TSS). We ranked the list according to the TF ChIP-chip signal and used it as input to DRIM. DRIM successfully detected the TFBS of these TFs that are reported in TRANSFAC with extremely significant p-values: HNF1α liver - GTTAMWNATT (P = 10^{-8}), HNF4α Islets - SCGGAAR (P = 10^{-53}), HNF6 Liver -

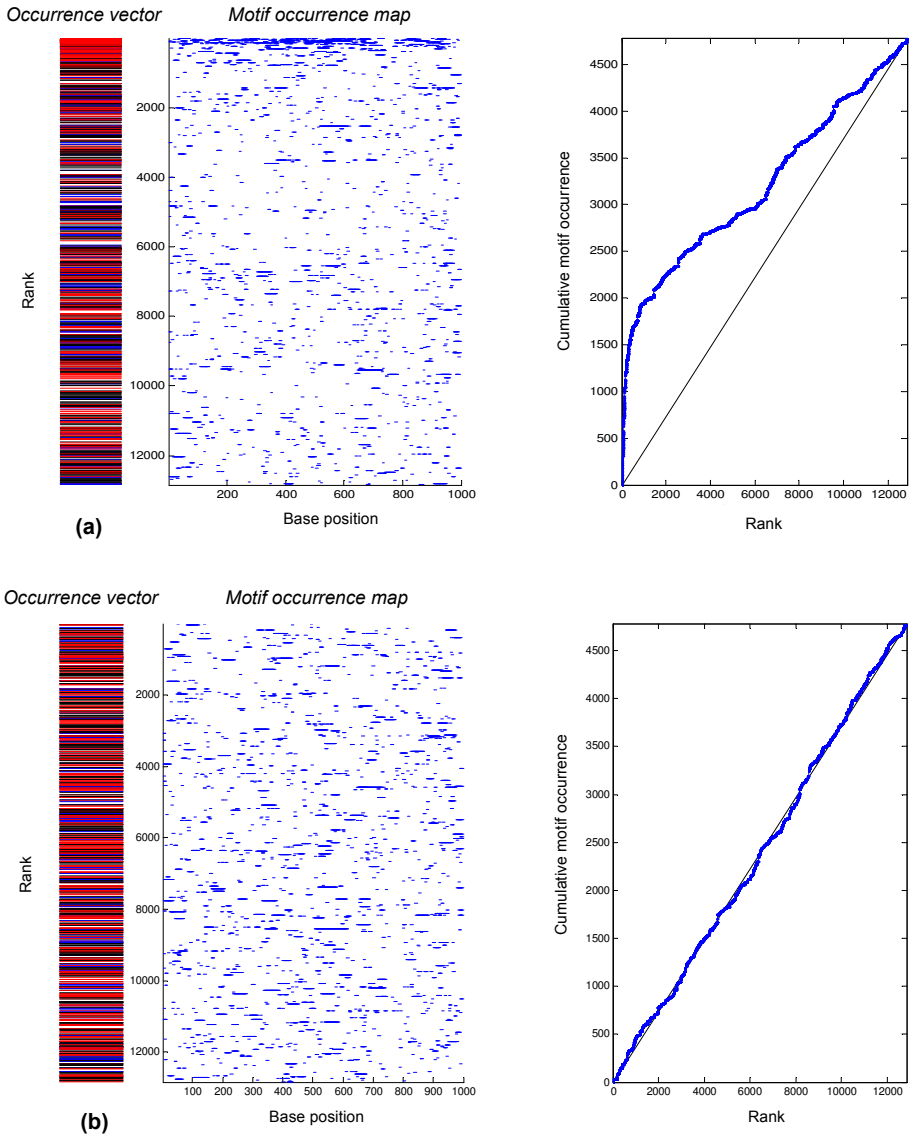

Figure 15: Occurrences of CA repeats in the human genome and their correlation to CpG methylation. (a) ∼13,000 promoters were ranked according to their CpG methylation in a human carcinoma cell-line [6]. Similarly to Figure 13 from left to right are the *occurrence vector*, *motif occurrence map* and the plot of the *cumulative motif occurrence*, all generated for the motif CACACACA. It can be seen that the CA repeats are highly correlated with CpG methylation as indicated by the increased density of the motif occurrences at the regions that are ranked top. (b) A control experiment in which the promoters are randomly ranked. It can be seen that the CA repeat occurrences are distributed uniformly and the observed cumulative motif occurrence is close to the expected.

ATCRAT (P = 10^{-57}) and HNF6 Islets - ATCRAT (P = 10^{-61}). In the CREB experiments we identified the palindromic motif TGACGTCA (P = 10^{-16}), which is known to bind CREB [57].

5.5 Comparison to other methods

Three properties of the mHG enrichment score embodied in DRIM offer advantages over other motif discovery methods: the dynamic cutoff; the rigorous control over false positives and the motif multiplicity model.

5.5.1 Dynamic vs. rigid cutoffs

Most methods use an arbitrary cutoff for set partition. For example, in previous work [1] the authors use a cutoff of p-value$<10^{-3}$ on the ChIP-chip signal in order to define the target set for motif searching. In contrast, the mHG score uses a data driven flexible cutoff and chooses the set partition that maximizes the motif enrichment.

To more systematically investigate the advantages of using a flexible cutoff we compared mHG with fixed set partition HG [16] by disabling the flexible cutoff feature in DRIM. The comparison was performed on ChIP-chip data of TFs whose motif binding sites are well characterized as well as on the Aro80 novel binding site (described in Section 5.2.1). For each TF we ranked the sequences according to the ChIP-chip binding signal, generated the motif occurrence vector and computed its HG enrichment using fixed target sets containing the top 10, 100, 1000 sequences as well as all sequences with ChiP-chip signal $< 10^{-3}$. The results are summarized in Figure 16. We note that all of the scores are corrected for multiple motif testing. The mHG score is also corrected for the multiple cutoff testing. The mHG method yields superior results in all 6 cases.

We performed additional comparisons of the mHG versus the HG methods by applying both methods to simulations of motif occurrence vectors (see Section 7.3). In these simulations mHG showed significantly better performance than HG.

To further investigate the issue of setting a cutoff we compare, for a given TF and condition in the ChIP-chip dataset, the number of promoters for which the binding signal $< 10^{-3}$ (denoted $\#(10^{-3})$) with the number of promoters at which mHG was attained (denoted n^*). For 82 experiments $\#(10^{-3}) \leq 4$ and for 46 of these $\#(10^{-3}) = 0$. In these cases a 10^{-3} fixed cutoff reduces the size of the target set and limits the usability of the any discovery algorithm. In Figure 17 we compare $\#(10^{-3})$ and n^* for some of the cases at which a motif was found by mHG. Note that in a significant number of cases the mHG score identified a significantly enriched motif even when $\#(10^{-3})$ was very low. One extreme case is the TF SOK2 in YPD condition for which $\#(10^{-3}) = 0$, yet mHG found a significantly enriched motif.

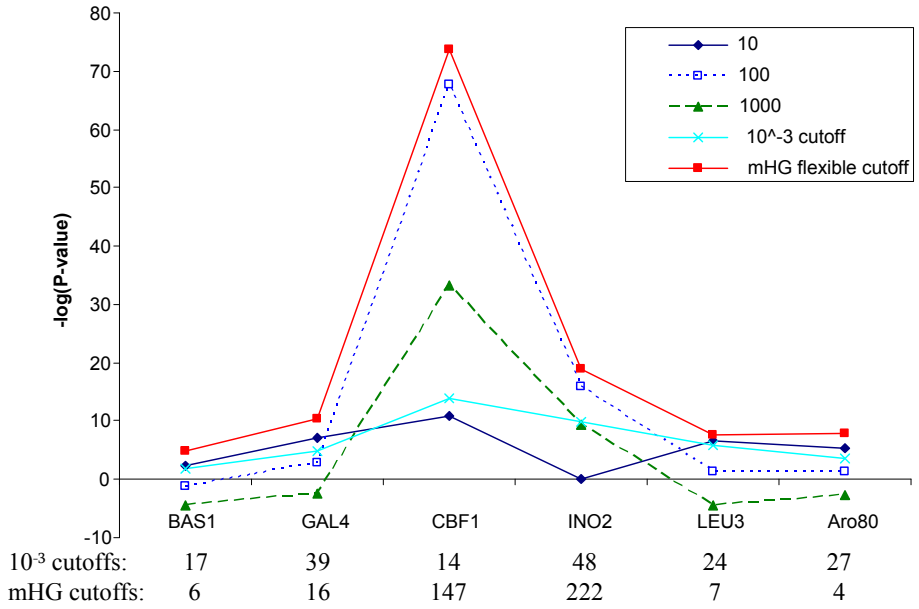

Figure 16: Comparison between HG and mHG enrichment. The mHG and HG methods were applied to ChIP-chip data of 6 TFs. The sequences were ranked according to the ChIP-chip binding signal and the enrichment of the correct binding motif was recorded using mHG and HG with fixed target sets containing the top 10, 100, 1000 sequences as well as all sequences with ChIP-chip signal $< 10^{-3}$. All scores were corrected for multiple motif testing. The mHG score is also corrected for the multiple cutoff testing. The 10^{-3} and mHG cutoffs for each experiment are shown. It can be seen that the two cutoffs are significantly different and that for all the tested TFs mHG produces better results than HG in terms of enrichment of the true motif.

5.5.2 Controlling false positives

The second advantageous property of the mHG score is its ability to rigorously control false positives, due to calculation of an exact p-value. This attribute is best demonstrated by comparing the performance of DRIM versus other motif finding tools on datasets whose original ranking was randomly permuted. It is clear that in these cases we should not find significantly enriched motifs. To this end we used the same benchmark on which DRIM was tested (Section 5.1). Using the same 5 random permutations of ChIP-chip data, we applied the algorithms AlignACE [21], MEME [17] and MDscan [48] on each of the random sets. Both AlignACE and MEME reported significant motifs with many A's, probably due to the existence of polyA tails in the intergenic regions. MDscan was used with a pre-compiled background from yeast intergenic regions, and therefore it did not report the polyA motifs, yet it did report motifs including repeats of TA, probably as a result of TATA boxes. In comparison, DRIM did not identify any significant results in any of the random sets.

5.5.3 Binary versus multi-dimensional enrichment

The third advantageous property, is the generalization of binary enrichment to enrichment above the natural numbers (Section 4.3). This type of enrichment forms a basis for dealing with motif multiplicity in a data

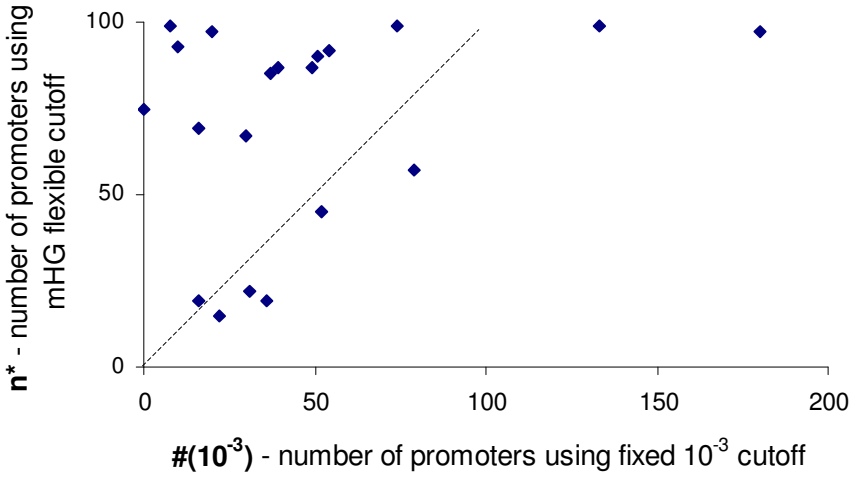

Figure 17: Comparison of the target sets sizes as determined by the fixed versus the mHG flexible cutoffs. Each dot represents a ChIP-chip experiment where the x and y coordinates are the number of promoters with $p < 10^{-3}$ (standard cutoff) and the number of promoters as determined by the mHG cutoff, respectively. The dotted line is $x = y$. TF names are given in Table S4

driven manner. To test this property we compared DRIM, which uses the multi-mHG framework, with a restricted version of DRIM, which uses the standard binary enrichment framework. Out of 31 binding motifs identified by DRIM that were also identified in other literature, the restricted version was able to identify only 23. Furthermore, in some instances both methods were able to identify the correct motif site, however the motif significance using the multi-mHG framework was several fold more significant without causing additional false predictions.

6 Discussion

In this paper we examine the problem of discovering "interesting" motif sequences in biological sequence data. While this problem has often been regarded as tantamount to discovering enriched motifs in a target set versus a background set, we point out an inherent limitation to this problem formulation. Specifically, in most cases, biological measurement data does not lend itself to such a clear partition into target and background sets in a data driven manner. It does, however, lend itself to ranking in a natural manner. Our approach exploits this natural ranking and attempts to solve challenges (c1)-(c4) discussed in Section 3.2.

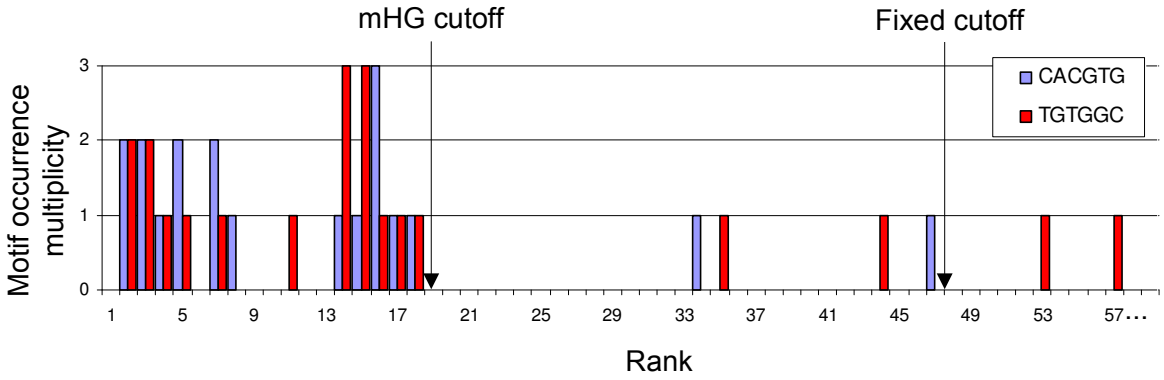

Figure 18: Motif occurrences in the top 59 (of ∼6000) promoters that were ranked according to Met32 binding signal. A comparison is made between the data driven mHG cutoff and the arbitrary fixed cutoff. It can be seen that the motifs are significantly more enriched when the list is partitioned using the mHG cutoff.

6.1 Addressing the four challenges of motifs discovery and future challenges

To address challenge (c1), instead of choosing an arbitrary cutoff for set partition, we search for a cutoff that partitions the data in a way that maximizes the motif enrichment. We present evidence that shows that the flexible mHG cutoff outperforms the rigid cutoff. One strong example of this is shown in Figure 16, where the flexible cutoff yields better results for all the TFs that were tested. Another example includes the discovery of previously undetected motifs such as that of the Aro80 (Section 5.2.1). Yet another example is the two motifs detected in 3 factors involved in the sulfur amino acid pathway (Met4, Met31 and Met32) (Section 5.2.3). Figure 18 shows the number of motif occurrences in each of the top 59 promoters that were ranked according to Met32 binding signal (data from [1]). The motifs are highly frequent in the top 18 promoters, after which a strong drop in motif frequency is observed. DRIM identifies this, and partitions the set accordingly. In comparison, relying on the standard cutoff of 10^{-3} results in a target set of the top 48 promoters, most of which do not contain this motif; this decreases the signal to noise ratio and may explain why these motifs were previously overlooked.

While the flexible cutoff is advantageous in many instances it also introduces a multiple testing problem. To circumvent this (without resorting to strict multiple testing corrections that may mask the biological signal) we developed an efficient algorithm for computing the exact mHG p-value. This addresses challenge (c2). Another advantage of this exact statistical score is its straight forward biological interpretation. Namely, the mHG p-value reflects the surprise of seeing the observed density of motif occurrences at the top of the ranked list under the null assumption that all configurations of motif occurrences are equiprobable.

Motif multiplicity is often indicative of biological function. It is therefore paramount to incorporate this type of information into the motif prediction model. We do so in a data driven manner by developing

the multi-mHG framework described in Section 4.3, thus addressing challenge (c3). The advantages of the multi-mHG model over the binary model are presented in Section 5.5, where the multi-mHG was able to identify true motifs that elude the binary model.

False prediction of motifs in randomly generated data is often mentioned as one of the drawbacks of computational motif discovery [1]. In Section 5.1 we report testing DRIM on random permutations of ranked sequences. When tested on more than 400,000 motifs, DRIM did not report any significant motifs, thus addressing challenge (c4). The same benchmark was applied to other methods (Section 5.5). All of the methods reported motifs with significant scores when applied to random sets of sequences. The low false positive prediction of our method is mainly attributed to the fact that it is based on rigorous statistics and relies on an exact p-value.

Another important issue that still requires consideration is the characterization of the motif search space. In this study we performed an exhaustive scanning of a restricted motif space (containing $\sim 10^5$ motifs) followed by a heuristic search for larger motifs (see Section 4.5). However, the motif search space can be further extended to include motifs that are longer, "fuzzier" or more complex. Additional considerations such as the distance of the motif from the transcription start site may be taken into account as well as logical relations between different motifs (e.g. 'OR', 'AND' operations). It is clear that many of these features are required to correctly model complex regulation patterns that are observed in higher eukaryotes. However, Two inherent limitations need to be considered when extending the search space: First, as the size of the motif search space increases the problem of efficiently searching the defined space becomes more acute in terms of running time. Second, since the size of the search space is virtually endless, the problem of multiple testing rapidly erodes the signal to noise ratio, requiring an appropriate refinement of the statistical models.

6.2 Sequence length bias in ChIP-chip data

A dataset containing the ChIP-chip data of all 203 putative TFs in Saccharomyces cerevisiae [1, 42] was constructed. Surprisingly we found that roughly third of these experiments had significantly longer sequences at the top of the ranked list, which means that for some TFs, longer sequences tend to get stronger TF binding signals. This observation is unexpected since, although longer probes hybridize more labeled material than shorter probes the increase is proportional in both channels. It might be caused by some bias in the ChIP-chip protocol. Alternatively, non-specific bindings between TFs and DNA may explain why longer sequences bind more TFs. This explanation is also consistent with the "TF sliding hypothesis" [58]. Why only some TFs exhibit this length bias binding tendency while others don't remains an open question. We note that this phenomenon may cause spurious results under our model assumptions and hence we filtered out all ChIP-chip experiments that had length bias.

6.3 Novel motifs in ChIP-chip data

We analyzed the ChIP-chip datasets using DRIM and identified 50 novel putative TFBS motifs that were previously undetected using 6 other computational methods run on the same data [1]. Next, we turned to assess whether these motifs have a biological function or, alternatively, they are a result of some bias in the data or statistical model. We found that 7 of these putative motifs have been previously identified using techniques other than ChIP-chip. Furthermore, 10 match conserved regulatory sites in yeast that were recently reported [45]. Taken together this is a strong indication that many of the new motifs DRIM is picking up on are true biological signals. We then turned to further analyze some of these motifs.

One interesting finding is that the Aro80 motif we identified, which exists only in 7 copies throughout the entire yeast genome, resides in Aro80's own promoter. This seems to suggest that Aro80 regulates its own transcription by binding to its own promoter. We also present a experimentally testable hypothesis to the regulation of the Aro80 pathway in Section 7.4.

Another interesting observation are the CA repeat motifs, which we identified in 7 different yeast TFs as well as in human DNA methylation. This type of low complexity motifs have so far been mostly ignored or filtered out by other computational methods. By contrast there is no need to resolve to this type of artificial filtering when using the mHG statistics. Our findings in yeast suggest that for certain TFs there is a significant correlation between a sequence's capacity to bind a TF and the presence of a CA repeat in the sequence. This supports a previous hypothesis that CA repeats alter the structure of DNA and thus contribute to TF binding [49]. Our findings constitute concrete examples of this phenomenon and suggest it may be more frequent than previously thought.

6.4 Novel motifs in CpG data

We also applied DRIM to high-throughput measurements of methylated CpG islands [6] in human cancer cells, in order to try and identify motifs that are enriched in hyper methylated regions. Interestingly, we identified GA and CA repeat elements as highly enriched in methylated CpG regions of 4 different cancer cell-lines. This is in agreement with previous studies of CpG methylated regions in other cell-lines [52, 53]. It is interesting to ask whether these repeat elements play some active role in the CpG methylation. In [53] the authors give statistical argumentation against such a hypothesis. Instead, they hypothesize that CA (or TG) repeats are caused by an increased mutation rate of methylated CpGs that are deaminated into TpGs. Even if true, this still does not explain the enrichment of the GA repeats. Further experimental and bioinformatics interrogation of this point is therefore called upon.

Overall, DRIM discovered 10 novel motifs in methylated CpG regions. Strikingly, 9 of them are similar

to DNA sequence elements that bind the Polycomb complex in drosophila and/or human [8, 9, 10]. The Polycomb complex is involved in epigenetic silencing via histone methylation. The suggested link between histone methylation and CpG methylation is in agreement with recent work that demonstrated the EZH2 protein interacts with DNA methyltransferases via the Polycomb complex [55]. We also note that the DNA sequence motifs of the two pathways were conserved in drosophila and human, which is complement to the observation that the Polycomb proteins are evolutionary conserved [59, 10]. Another interesting observation is that many of the motifs we found in the CpG methylated data are similar across different types of cancer-cells. This may suggest that the CpG methylation mechanism is orchestrated by DNA binding factors that are similar in different types of cancer-cells.

6.5 Concluding remarks

Perhaps the most important conclusion that can be drawn from this study is that looking at biological sequence data in a ranked manner rather than using an arbitrary fixed cutoff to partition the data enables the detection of biological signals that are otherwise overlooked. This suggests that other motif detection methods that rely on fixed cutoffs may benefit from dynamic partitioning. While the effectiveness of our approach was demonstrated mainly on ChIP-chip and methylation data it can also be applied to a wide range of other data types such as expression data or GO analysis (for details see Section 7.5). The DRIM application is publicly available at: http://bioinfo.cs.technion.ac.il/drim.

References

[1] C.T. Harbison, D.B. Gordon, T.I. Lee, N.J. Rinaldi, K.D. Macisaac, T.W. Danford, N.M. Hannett, J.B. Tagne, D.B. Reynolds, J. Yoo, E.G. Jennings, J. Zeitlinger, D.K. Pokholok, M. Kellis, P.A. Rolfe, K.T. Takusagawa, E.S. Lander, D.K. Gifford, E. Fraenkel, and R.A. Young. Transcriptional regulatory code of a eukaryotic genome. *Nature*, 431(17004):99–104, 2004.

[2] J. Gorodkin, L. J. Heyer, S. Brunak, and G. D. Stormo. Displaying the information contents of structural RNA alignments: the structure logos. *Computer Applications in Biosciences*, 13:583–586, 1997.

[3] I. Iraqui, S. Vissers, B. Andre, and A. Urrestarazu. Transcriptional induction by aromatic amino acids in Saccharomyces cerevisiae. *Molecular Cell Biology*, 19:3360–3371, 1999.

[4] PL. Blaiseau and D. Thomas. Multiple transcriptional activation complexes tether the yeast activator Met4 to DNA. *EMBO*, 17:6327–6336, 1998.

[5] PL. Blaiseau, AD. Isnard, Y. Surdin-Kerjan, and D. Thomas. Met31p and Met32p, two related zinc finger proteins, are involved in transcriptional regulation of yeast sulfur amino acid metabolism. *Molecular Cell Biology*, 17:3640–3648, 1997.

[6] I. Keshet, Y. Schlesinger, S. Farkash, E. Rand, M. Hecht, E. Segal, E. Pikarski, RA. Young, A. Niveleau, H. Cedar, and I. Simon. Evidence for an instructive mechanism of de novo methylation in cancer cells. *Nature Genetics*, 38:149–153, 2006.

[7] M.M. Kittleson, K.M. Minhas, R.A. Irizarry, S.Q. Ye, G. Edness, E. Breton, J.V. Conte, G. Tomaselli, J.G. Garcia, and J.M. Hare. Gene expression analysis of ischemic and nonischemic cardiomyopathy: Shared and distinct genes in the development of heart failure. *Physiol Genomics*, 21:299–307, 2005.

[8] L. Ringrose, M. Rehmsmeier, JM. Dura, and R. Paro. Genome-wide prediction of polycomb/trithorax response elements in Drosophila melanogaster. *Developmental cell*, 5:759–771, 2003.

[9] T.I. Lee, RG. Jenner, LA. Boyer, MG. Guenther, SS. Levine, RM. Kumar, B. Chevalier, SE. Johnstone, MF. Cole, K. Isono, H. Koseki, T. Fuchikami, K. Abe, HL. Murray, JP. Zucker, B. Yuan, GW. Bell, E. Herbolsheimer, NM. Hannett, K. Sun, DT. Odom, AP. Otte, TL. Volkert, DP. Bartel, DA. Melton, DK. Gifford, R. Jaenisch, and RA. Young. Control of developmental regulators by polycomb in human embryonic stem cells. *Cell*, 125:301–313, 2006.

[10] AP. Bracken, N. Dietrich, D. Pasini, KH. Hansen, and K. Helin. Genome-wide mapping of polycomb target genes unravels their roles in cell fate transitions. *Genes and Development*, 20:1123–1136, 2006.

[11] B. Ren, F. Robert, J.J. Wyrick, O. Aparicio, E.G. Jennings, I. Simon, J. Zeitlinger, J. Schreiber, N. Hannett, E. Kanin, T.L. Volkert, C.J. Wilson, S.P. Bell, and R.A. Young. Genome-wide location and function of DNA binding proteins. *Science*, 290(5500):2306–9, 2000.

[12] H.J. Bussemaker, H. Li, and E.D. Siggia. Regulatory element detection using correlation with expression. *Nature Genetics*, 27:167–71, 2001.

[13] S. Sinha and M. Tompa. Discovery of novel transcription factor binding sites by statistical overrepresentation. *Nucleic Acids Research*, 30:5549–5560, 2002.

[14] S. Sinha and M. Tompa. Ymf: a program for discovery of novel transcription factor binding sites by statistical overrepresentation. *Nucleic Acids Research*, 31:3586–3588, 2003.

[15] C.T Workman and G.D Stromo. ANN-SPEC: a method for discovering transcription factor binding sites with improved specificity. *Pacific Symposium on Biocomputing*, 5:464–475, 2000.

[16] Y. Barash, G. Bejerano, and N. Friedman. A simple hyper-geometric approach for discovering putative transcription factor binding sites. *Lecture Notes in Computer Science*, 2149, 2001.

[17] T.L. Bailey and C. Elkan. Fitting a mixture model by expectation maximization to discover motifs in biopolymers. In *Proceedings of ISMB*, pages 28–36. 1994.

[18] X. Liu, DL. Brutlag, and JS. Liu. Bioprospector: discovering conserved DNA motifs in upstream regulatory regions of co-expressed genes. *Pac Symp Biocomput*, pages 127–138, 2001.

[19] P. Hong, X. S. Liu, Q. Zhou, X. Lu, J. S. Liu, and W. H. Wong. A boosting approach for motif modeling using ChIP-chip data. *Bioinformatics*, 21:2636–2643, 2005.

[20] A. D. Smith, D. Sumazin, P. abd Das, and M. Q. Zhang. Mining ChIP-chip data for transcription factor and cofactor binding sites. *Bioinformatics*, 21:408–412, 2005.

[21] F.P. Roth, J.D. Hughes, P.W. Estep, and G.M. Church. Finding DNA regulatory motifs within unaligned noncoding sequences clustered by whole-genome mRNA quantitation. *Nature Biotechnology*, 16(10):939–945, 1998.

[22] I. Ben-Gal, A. Shani, A. Gohr, J. Grau, S. Arviv, A. Shmilovici, S. Posch, and I. Grosse. Identification of transcription factor binding sites with variable-order Bayesian networks. *Bioinformatics*, 21:2657–2666, 2005.

[23] Y. Barash, G. Elidan, N. Friedman, and T. Kaplan. Modeling dependencies in protein-dna binding sites. *RECOMB*, 2003.

[24] S. Sinha and M. Tompa. A statistical method for finding transcription factor binding sites. *ISMB*, 2000.

[25] M. Tompa, N. Li, T.L. Bailey, G.M. Church, B. De Moor, E. Eskin, A.V. Favorov, M.C. Frith, Y. Fu, W.J. Kent, V.J. Makeev, A.A. Mironov, W.S. Noble, G. Pavesi, G. Pesole, M. Regnier, N. Simonis, S. Sinha, G. Thijs, J. van Helden, M. Vandenbogaert, Z. Weng, C. Workman, C. Ye, , and Z. Zhu. Assessing computational tools for the discovery of transcription factor binding sites. *Nature Biotechnology*, 23(1):137–144, 2005.

[26] KD. MacIsaac and E. Fraenkel. Practical strategies for discovering regulatory DNA sequence motifs. *PLOS Computational Biology*, 2:201–210, 2006.

[27] J. Hu, B. Li, and D. Kihara. Limitations and potentials of current motif discovery algorithms. *Nucleic Acids Research*, 33:4899–4913, 2005.

[28] ML. Bulyk. Computational prediction of transcription-factor binding site locations. *Genome Biology*, 5, 2003.

[29] M. Friberg, P. von Rohr, and G. Gonnet. Scoring functions for transcription factor binding site prediction. *BMC Bioinformatics*, 6, 2005.

[30] D. Das, Z. Nahle, and M. Q. Zhang. Adaptively inferring human transcriptional subnetworks. *Molecular Systems Biology*, 2006.

[31] S. Sinha, Y. Liang, and E. Siggia. Stubb: a program for discovery and analysis of cis-regulatory modules. *Nucleic Acids Research*, 34:555–559, 2006.

[32] W. Thompson, EC. Rouchka, and C. E. Lawrence. Gibbs recursive sampler: finding transcription factor binding sites. *Nucleic Acids Research*, 31:3580–3585, 2003.

[33] O. Hallikas, K. Palin, N. Sinjushina, R. Rautiainen, J. Partanen, E. Ukkonen, and J. Taipale. Genome-wide prediction of mammalian enhancers based on analysis of transcription-factor binding affinity. *Cell*, 124:47–59, 2006.

[34] M. Gupta and JS. Liu. De novo cis-regulatory module elicitation for eukaryotic genomes. *PNAS*, 102:7079–7084, 2005.

[35] LJ. Jensen and S. Knudsen. Automatic discovery of regulatory patterns in promoter regions based on whole cell expression data and functional annotation. *Bioinformatics*, 16:326–333, 2000.

[36] C. Ben-Zaken Zilberstein, E. Eskin, and Z. Yakhini. Using expression data to discover RNA and DNA regulatory sequence motifs. In *The First Annual RECOMB Satellite Workshop on Regulatory Genomics*. 2004.

[37] A. Ben-Dor, L. Bruhn, N. Friedman, I. Nachman, M. Schummer, and Z. Yakhini. Tissue classification with gene expression profiles. *Journal of Computational Biology*, 2000.

[38] M. Bittner, P. Meltzer, Y. Chen, Y. Jiang, E. Seftor, M. Hendrix, M. Radmacher, R. Simon, Z. Yakhini, A. Ben-Dor, N. Sampas, E. Dougherty, E. Wang, F. Marincola, C. Gooden, J. Lueders, A. Glatfelter, P. Pollock, J. Carpten, E. Gillanders, D. Leja, K. Dietrich, C. Beaudry, M. Berens, D. Alberts, and V. Sondak. Molecular classification of cutaneous malignant melanoma by gene expression profiling. *Nature*, 406(6795):536–40, 2000.

[39] A. Ben-Dor, N. Friedman, and Z. Yakhini. Scoring genes for relevance. Technical Report 2000-38, School of Computer Science & Engineering, Hebrew University, Jerusalem, 2000. See http://www.cs.huji.ac.il/∼nir/Abstracts/BFY1.html.

[40] E.I. Boyle, S. Weng, J. Gollub, H. Jin, D. Botstein, J. M. Cherry, and G. Sherlock. Go::termfinderopen source software for accessing gene ontology information and finding significantly enriched gene ontology terms associated with a list of genes. *Bioinfromatics*, 20:3710–3715, 2004.

[41] M.J. Buck and Lieb J.D. ChIP-chip: considerations for design, analysis, and application of genome-wide chromatin immunoprecipitation experiments. *Genomics*, 83:349–60, 2003.

[42] T.I. Lee, N.J. Rinaldi, F. Robert, D.T. Odom, Z. Bar-Joseph, G.K. Gerber, N.M. Hannett, C.T. Harbison, C.M. Thompson, I. Simon, J. Zeitlinger, Jennings E.G., H.L. Murray, D.B. Gordon, Bin Ren, J.J Wyrick, J.B. Tagne, T.L. Volkert, E. Fraenkel, D.K. Gifford, and R.A. Young. Transcriptional regulatory networks in Saccharomyces cerecisiae. *Science*, 298:799–804, 2002.

[43] H. Shi, S. Maier, I. Nimmrich, P. Yan, C.W. Caldwell, A. Olek, and Huang T.H.I. Oligonucleotide-based microarray for DNA methylation analysis: principles and applications. *Journal of Cellular Biochemistry*, 88:138–143, 2003.

[44] Z. Zhu, Y. Pilpel, and GM. Church. Computational identification of transcription factor binding sites via a transcription-factor-centric clustering (tfcc) algorithm. *J. Molecular Biology*, 318:71–81, 2002.

[45] K.D. MacIsaac, T. Wang, B.D. Gordon, D.K. Gifford, G.D. Stromo, and E. Fraenkel. An improved map of conserved regulatory sites for Saccharomyces cerevisiae. *BMC bioniformaitcs*, 7, 2006.

[46] Z. Vuralhan, MA. Morais, SL. Tai, MD. Piper, and JT. Pronk. Identification and characterization of phenylpyruvate decarboxylase genes in Saccharomyces cerevisiae. *Applied and Environmental Microbiology*, 69:4534–4541, 2003.

[47] MM. Etschmann, W. Bluemke, D. Sell, and J. Schrader. Biotechnological production of 2-phenylethanol. *Applied microbiology and biotechnology*, 59:1–8, 2002.

[48] X.S. Liu, D.L. Brutlag, and J.S. Liu. An algorithm for finding protein-DNA binding sites with applications to chromatin-immunoprecipitation microarray experiments. *Nature Biotechnology*, 20:835–39, 2002.

[49] R. Nussinov. Some guidelines for identification of recognition sequences: regulatory sequences frequently contain (t)gtg/cac(a), tga/tca and (t)ctc/gag(a). *Biochimica et biophysica acta*, 866:93–108, 1986.

[50] NP. Anagnou, AD. Moulton, G. Keller, S. Karlsson, T. Papayannopoulou, G. Stamatoyannopoulos, and AW. Nienhuis. Cis-acting sequences that affect the expression of the human fetal gamma-globin genes. *Progress in clinical and biological research*, 191:163–182, 1985.

[51] SF. Anderson, CM. Steber, RE. Esposito, and JE. Coleman. Ume6, a negative regulator of meiosis in Saccharomyces cerevisiae, contains a c-terminal Zn2Cys6 binuclear cluster that binds the URS1 DNA sequence in a zinc-dependent manner. *Protein Science*, 4:1832–1843, 1995.

[52] F. A. Feltus, E. K. Lee, J. F. Costello, C. Plass, and P. M. Vertino. Predicting aberrant CpG islands methylation. *PNAS*, 100:12253–1258, 2003.

[53] C. Bock1, M. Paulsen, S. Tierling, T. Mikeska, T. Lengauer, and J. Walter. CpG island methylation in human lymphocytes is highly correlated with DNA sequence, repeats, and predicted DNA structure. *PLoS Genetics*, 2:243–252, 2006.

[54] H. Strutt, Cavalli. G., and R. Paro1. Co-localization of polycomb protein and GAGA factor on regulatory elements responsible for the maintenance of homeotic gene expression. *EMBO Journal*, 16:3621–3632, 1997.

[55] E. Vire, C. Brenner, R. Deplus, L. Blanchon, M. Fraga, C. Didelot, L. Morey, A. Van Eynde, D. Bernard, JM. Vanderwinden, M. Bollen, M. Esteller, L. Di Croce, Y. de Launoit, and F Fuks. The polycomb group protein EZH2 directly controls DNA methylation. *Nature*, 439:871–874, 2006.

[56] D.T. Odom, N. Zizlsperger, D.B. Gordon, G.W. Bell, N.J. Rinaldi, H.L. Murray, T.L. Volkert, J. Schreiber, P.A. Rolfe, D.K. Gifford, E. Fraenkel, G.I. Bell, and R.A. Young. Control of pancreas and liver gene expression by hnf transcription factors. *Science*, 303:1378–1381, 2004.

[57] X. Zhang, DT. Odom, SH. Koo, MD. Conkright, G. Canettieri, J. Best, H. Chen, R. Jenner, E. Herbolsheimer, E. Jacobsen, S. Kadam, JR. Ecker, B. Emerson, JB. Hogenesch, T. Unterman, RA. Young, and M. Montminy. Genome-wide analysis of camp-response element binding protein occupancy, phosphorylation, and target gene activation in human tissues. *PNAS*, 102:4459–4464, 2005.

[58] C. Deremble and R Lavery. Macromolecular recognition. *Current opinion in structural biology*, 15:171–175, 2005.

[59] SS. Levine, A. Weiss, H. Erdjument-Bromage, Z. Shao, P. Tempst, and RE. Kingston. The core of the polycomb repressive complex is compositionally and functionally conserved in flies and humans. *Molecular and Cellular Biology*, 22:6070–6080, 2002.

[60] M. Ashburner, CA. Ball, J.A. Blake, D. Botstein, H. Butler, JM. Cherry, AP. Davis, K. Dolinski, SS. Dwight, J.T. Eppig, M.A. Harris, L. Hill, D.P. Issel-Tarver, A. Kasarskis, S. Lewis, J.C. Matese, J.E. Richardson, M. Ringwald, G.M. Rubin, and G. Sherlock. Gene ontology: tool for the unification of biology. the gene ontology consortium. *Nature Genetics*, 25:25–29, 2000.

[61] R.S. Sealfon, M.A. Hibbs, C. Huttenhower, C.L. Myers, and O.G. Troyanskaya. Golem: an interactive graph-based gene-ontology navigation and analysis tool. *BMC Bioinformatics*, 7, 2006.

[62] R.G. Emden and C.N. Stephen. An open graph visualization system and its applications to software engineering. *Software Practice and Expirience*, pages 1–5, 1999.

7 Appendix I - Supplementary material

7.1 Bounds for the mHG p-value

We demonstrate several bounds for pVal(p). These bounds may be used for rapid assessment of the p-value of a given mHG score, which can be instrumental in improving algorithmic efficiency. In Figure S1 we compare the bounds with exact p-values as well as with observed frequencies, on randomly generated test cases.

For fixed values of N and B we define $\text{HGT}_n(\lambda) = \text{HGT}(b_n(\lambda); N, B, n)$. $\text{HGT}(x; N, B, n)$ is the complement of the cumulative distribution function of a hypergeometric random variable. As such, for any value p we have $\text{Prob}(\text{HGT}_n(\lambda) \leq p) \leq p$ [1]. Set an attainable mHG score p. If $\text{mHG}(\lambda) = p$ then there is some rank n^* at which this score was attained. Clearly $\{\lambda : \text{HGT}_n(\lambda) \leq p\} \subseteq \{\lambda : \text{mHG}(\lambda) p\}$. For similar reasons $\{\lambda : \text{mHG}(\lambda) \leq p\} = \bigcup_{n=1}^{N} \{\lambda : \text{HGT}_n(\lambda) \leq p\}$. This leads to the following (trivial) bounds for any $\text{HGT}_n(\lambda)$ attainable p:

$$p \leq \text{Prob}(\text{mHG}(\lambda) \leq p) \leq Np. \quad [2] \tag{18}$$

In many cases the upper bound provided in (18) is very loose. When $B << N$ the following tighter upper bound is of greater use (see Figure S1). Fix N and B, and consider the space of all binary label vectors with B 1's and $N - B$ 0's: $\Lambda = \{0, 1\}^{(N-B,B)}$, endowed with a uniform probability measure.

Theorem 7.1 *For any $HGT_n(\lambda)$ attainable p:*

$$p \leq \textit{Prob}(\textit{mHG}(\lambda) \leq p) \leq Bp. \tag{19}$$

Proof: Note that we only need to test B thresholds to compute $\text{mHG}(\lambda)$. A union bound may therefore seem applicable. However, since the thresholds depend on the point λ and may be different for different λs we need to use a more careful argument.

For each $1 \leq i \leq B$ let n_i be the maximal rank n for which any vector $\lambda \in \Lambda$ with $b_n(\lambda) \geq i$ has a score $\text{HGT}_n(\lambda) \leq p$. Formally:

$$n_i = \max \{n : (b_n(\lambda) \geq i) \Rightarrow \text{HGT}_n(\lambda) \leq p\}. \tag{20}$$

Monotonicity properties of the hypergeometric distribution imply the existence of such numbers n_i. By definition they are constants, independent of λ.

[1] If X and Z are discrete random variables that take a finite number of values $X_1 \leq X_2 ... \leq X_k$ and $Z_1 \leq Z_2 ... \leq Z_m$ with probabilities $\Omega_1 = \{p_1, p_2 ... p_k\}$ and $\Omega_2 = \{q_1, q_2 ... q_m\}$ respectively, and $P(Z = x) = P(X \geq x)$ then the following properties hold: (1) $\forall$ p $P(Z \leq p) \leq p$; (2) for any attainable $p \in \Omega_2$ $P(Z \leq p) = p$.

[2] $p = \text{Prob}(\text{HGT}_n(\lambda) \leq p) \leq \text{Prob}(\text{mHG}(\lambda) \leq p) = \text{Prob}(\bigcup_{n=1}^{N} \{\lambda : \text{HGT}_n(\lambda) \leq p\}) \leq \sum_{n=1}^{N} \text{Prob}(\text{HGT}_n(\lambda) \leq p) \leq Np.$

Any vector λ for which $\text{mHG}(\lambda) \leq p$ attains this score at some rank $n^* = n^*(\lambda)$ (i.e. $\text{mHG}(\lambda) = \text{HGT}_{n^*}(\lambda)$). Let $b^* = b_{n^*}(\lambda)$. By definition (20) $n_{b^*} \geq n^*$ and therefore $b_{n_{b^*}}(\lambda) \geq b_{n^*}(\lambda) = b^*$ (the left hand side represents a larger prefix of the vector). Therefore, again from definition (20): $(\text{HGT}_{n_{b^*}}(\lambda) \leq p)$.

The above shows, in other words, that for any vector λ for which $\text{mHG}(\lambda) \leq p$ there is some value $1 \leq i \leq B$ (namely $i = b^*$) for which $\text{HGT}_{n_i}(\lambda) \leq p$. Note that even though this i depends on λ there are only B possible values and only B numbers n_i. Therefore:

$$\{\lambda : \text{mHG}(\lambda) \leq p\} \subseteq \bigcup_{i=1}^{B} \{\lambda : \text{HGT}_{n_i}(\lambda) \leq p\}\,, \tag{21}$$

and we can now apply a union bound to conclude:

$$\text{Prob}(\text{mHG}(\lambda) \leq p) \leq Bp. \qquad \diamondsuit \tag{22}$$

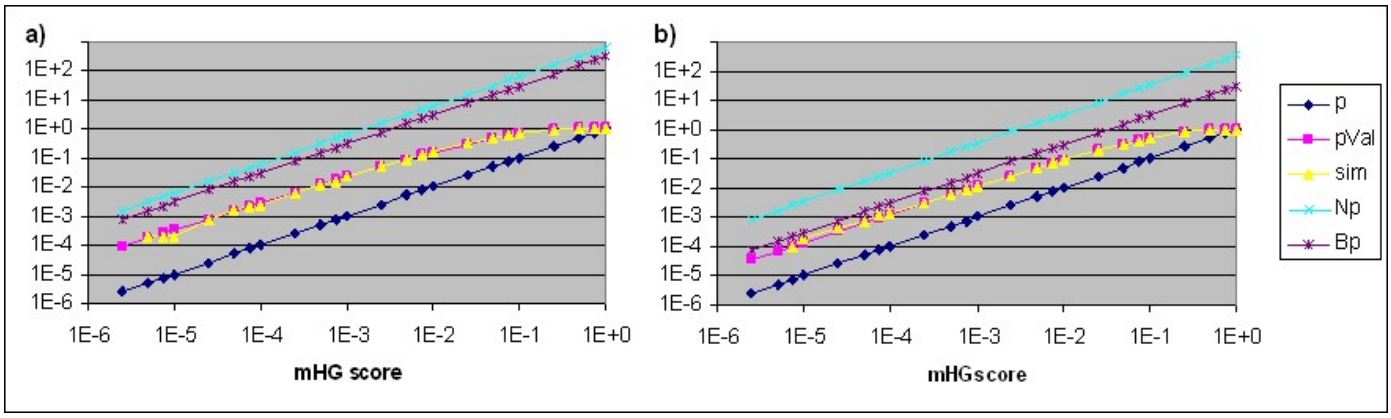

Figure S1: Comparison of p-value bounds, exact p-value calculation and observed frequencies of mHG scores for two synthetic cases: a) $N = 600$, $B = 300$, b) $N = 330$, $B = 30$. In each case the following values were generated for several different mHG scores: lower bound (p), trivial upper bound (Np), tighter upper bound(Bp), exact p-value calculation (pVal) and observed p-values over 10,000 random instances (sim). Note the improvement of the tighter upper bound (Bp) when $N >> B$.

7.2 How to compute the mHG score efficiently on trinary vectors

The following recursive formulas expand the ideas presented in Section 4.5.2 and explain how to efficiently compute the HG and HGT scores on a trinary vector. Formally, let λ be a trinary vector such that $\lambda = \lambda_1, ..., \lambda_N \in \{0, 1, 2\}^N$. Then:

$$HG(n+1, y, b, Y, B, N) = HG(n, y, b, Y, B, N) \cdot \frac{(n+1)(N-n-Y+y-B+b)}{(n+1-y-b)(N-n)}, \tag{23}$$

$$HG(n+1, y+1, b, Y, B, N) = HG(n, y, b, Y, B, N) \cdot \frac{(n+1)(Y-y)}{(y+1)(N-n)}, \tag{24}$$

$$HG(n+1,y,b+1,Y,B,N) = HG(n,y,b,Y,B,N) \cdot \frac{(n+1)(B-b)}{(b+1)(N-n)}, \tag{25}$$

where N is the size of λ; B and Y are the total number of 1's and 2's in λ; y and b are the number of 1's and 2's in $\lambda_1, ..., \lambda_n$.

A similar approach is used to compute the HGT using the following recursive formulas:

$$HG(n,y+1,b,Y,B,N) = HG(n,y,b,Y,B,N) \cdot \frac{(n-y-b)(Y-y)}{(y+1)(N-n-Y+y+1-B+b)} \tag{26}$$

$$HG(n,y,b+1,Y,B,N) = HG(n,y,b,Y,B,N) \cdot \frac{(n-y-b)(B-b)}{(b+1)(N-n-Y+y+1-B+b)} \tag{27}$$

7.3 Comparing mHG and HG on simulated motif occurrences

To further assess the properties of mHG compared to fixed set partition HG we performed a series of simulations in which the different methods were tested on random motif occurrence vectors, each generated according to a predefined distribution. When generating the occurrence vectors we tried to mimic occurrence vectors that arise from biological data. We define the probability of observing a motif occurrence at rank r in a vector as:

$$P = u + e^{-(a+r)b} \tag{28}$$

The parameter u is the probability of observing a motif independent of its position in the vector. This attempts to capture the background genomic noise.The exponent component in the equation decays as the vector rank increases. The parameters a and b control the rank-imbalance degree of the motif. For example, if b is fixed, the larger a the weaker the motif signal is.

We generated vectors with different parameter combinations. For each vector we computed the mHG p-value, and the HG p-value using the top 10, 100 and 1000 positions in the vector as a target set. The fraction between the mHG and the best HG p-value was recorded. Results are summarized in Figure S2. It can be see that in most cases the mHG p-value is equal or better than that of the HG .

7.4 Hypothesis: Aro80 network is inhibited by GATA binding factors

One interesting observation is that the BS_{Aro80} element in the Aro80 promoter region has three GATA binding sites that reside within its unconserved bases or adjacent to it, see Figure 11b. Upstream GATA binding sites have been shown to be involved in nitrogen catabolite repression. This gives rise to our following hypothesis: Aro80 regulates its own expression by binding to its own promoter region via the BS_{Aro80} element thus generating a positive feedback loop. Aro80 also binds to the promoters of Aro9 and Aro10 and Esbp6.

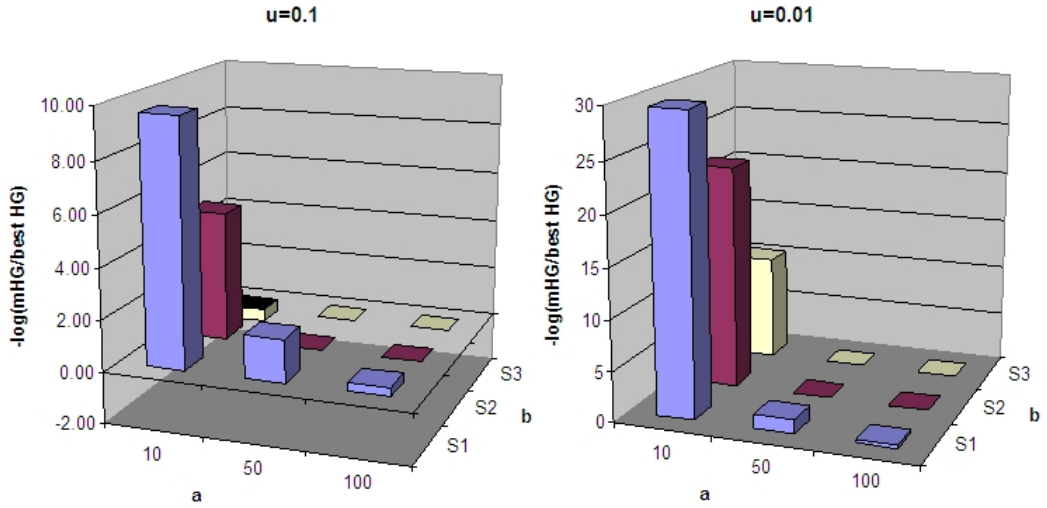

Figure S2: Comparison of the mHG and HG methods on simulations of motif occurrence vectors. The vectors were generated according to a rank dependent distribution (Section 7.3) with 18 different parameter combinations ($a = 10, 50, 100; b = 0.01, 0.05, 0.1; u = 0.01, 0.1$). The -log fraction between mHG and HG p-values in cases where the p-value of one of the methods was smaller than 10^{-3} are shown.

The inhibition of the system is achieved via GATA binding factors that bind near BS_{Aro80} in the Aro80 promoter. Consequentially the BS_{Aro80} binding element becomes inaccessible to Aro80. This breaks the positive feedback loop, which in turn reduces the amount of Aro80 and therefore indirectly inhibits the expression of Aro9, Aro10 and Esbp6. The entire mechanism is summarized in Figure 11.

We found further substantiation of this hypothesis when comparing the ChIP-chip data of Aro80 in rich media against SM (amino acid starvation) condition . In rich media, Aro80 binds strongest to the promoters of Aro9, Aro10, Esbp6 and Aro80. Under SM condition we would expect the Aro80 mediated pathway to be inhibited since the aromatic amino acid substrate is absent. Indeed, under SM condition, the binding capacity of all 4 promoters significantly drops. However, Aro9, Aro10 and Esbp6 promoters still retain the strongest binding capacity compared to the rest of the promoters, suggesting that the reduction in binding is achieved indirectly as a result of less Aro80 in the cell. In contrast, the binding capacity of Aro80 to the Aro80 promoter drops, not only in absolute terms, but also relative to other promoters in the ranked list (from rank 4 to rank 30 in YPD and SM respectively). This supports our hypothesis that the Aro80 access to its own promoter is directly prevented, presumably due to the GATA binding elements.

7.5 mHG and GO analysis

In the following section we briefly describe another mHG based application, termed GOviz, for analysis and graphical visualization of enriched GO terms in ranked lists of genes.

Recent advances in molecular biology high-throughput technologies (as microarray, ChIP-chip or mDIP) enable thousands of measurements in a single experiment. Such experiments often produce large lists of genes that are somehow associated (e.g. a list of genes with similar expression patterns). It is interesting to try and identify whether there is a common theme or biological phenomenon that links those genes. The Gene Ontology (GO) Consortium [60] is an ongoing effort aimed at providing controlled vocabularies, which associate genes with GO terms that fall into 3 categories: *Biological Process*, *Molecular Function* and *Cellular Component*. The GO terms are structured in DAGs (directed acyclic graphs) that capture the relations and dependencies between the terms [60]. A GO term that is over-represented in the target list of genes may reveal new insight and common functional characteristics of the genes in the list.

Several excellent tools have been developed for discovering GO terms that are enriched in lists of genes including [40, 61]. These tools search for enriched GO terms in a target set versus a background set of genes using the HG model or a binomial approximation of HG [40].

Following the same rational we used for enrichment of sequence motifs, we argue that it is possible to exploit the inherent ranking property of genomic measurements in order to enhance GO term enrichment analysis. Instead of using the HG model on fixed sets of genes we developed a GO analysis tool that computes GO term enrichment in ranked lists of genes using the mHG statistical framework. Two principle issues were at the focus of the GOviz tool design: (i) ease of usage and (ii) intuitive and easy interpretation of the results. To enable a straight-forward usage, the GOviz tool has an internal translator, which converts between the user inputted gene accessions to the accessions used in the GO database in a seeming-less manner. The tool is highly optimized - $\sim$10 seconds for running on a list containing $\sim$10,000 genes on a Pentium IV, 2Ghz, 512 RAM machine. GO analysis tools often return long lists of enriched GO terms, which do not lend themselves to easy interpretation. We developed a graphical representation of the GO analysis results that attempts to overcome this issue. The enriched GO terms (with mHG p-value better then a user predefined threshold) and all their ancestors in the GO DAG are visualized using a colored graph, where the colors of the nodes reflect the GO term enrichment. An example of the graphical output is shown in Figure S3. The graph is also clickable and enables easy retrieval of additional information such as genes that are associated with the enriched GO terms. The tool is implemented in C++ and Perl and invokes Graphviz, an open source graph visualization software [62]. The tool is publicly available at http://bioinfo.cs.technion.ac.il/GOviz.

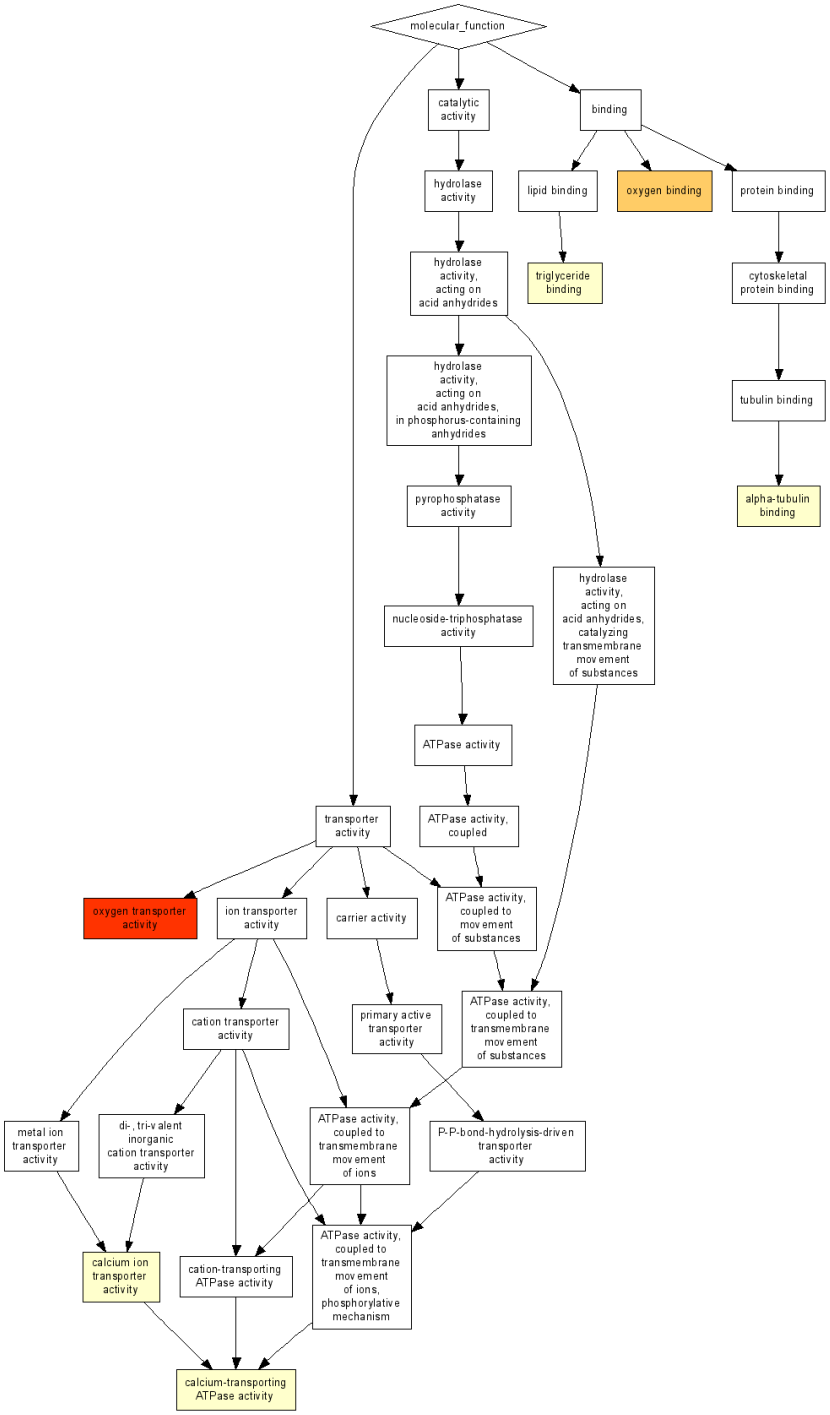

Figure S3: An example of the output of GOviz. A set of genes were ranked according to differential expression of 31 patients with CVD (cardio-vascular disease, either ischemic or non-ischemic) versus 6 patients with none failure hearts as reported in [7]. The enriched GO terms (mHG p-value $< 10^{-2}$ after bonfferoni correction for multiple GO term testing) and their parent GO terms up to the root are shown. The colors reflect the level of enrichment (yellow: 10^{-2} to 10^{-4}, orange: 10^{-4} to 10^{-6}, red: 10^{-6} to 10^{-8}) .

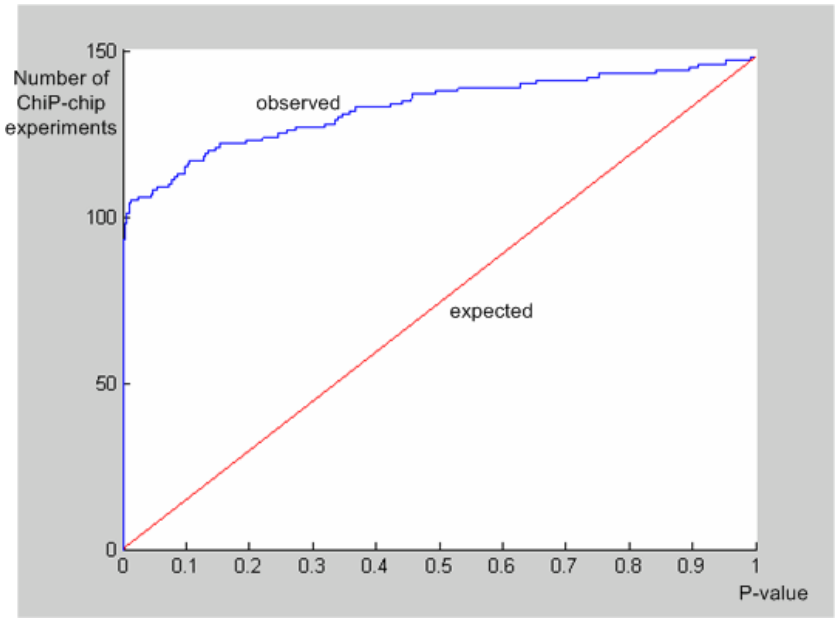

Figure S4: Observed versus expected length bias. For each of the 148 OC ChIP-chip experiments reported in [1] we ranked the yeast intergenic sequences according to their binding signal. The lengths of the top 300 sequences in each experiment were compared to the lengths of the rest of the sequences using a student t-test. The x axis is the t-test p-value and $y(x)$ is the number of TF experiments with $p \leq x$. The blue line is the observed cumulative distribution of the t-test p-values in the 148 experiments. The red line is the expected cumulative distribution of t-test p-values in randomly permuted sequence rankings. It can be seen that over half of the ChIP-chip experiments have a statistically significant difference between the lengths of sequences that bind the TF the strongest compared to the lengths of the rest of the sequences.

Table S1

The list of TFs in the Harbison filtered data set.

`Harbison filtered data set' -

TFs for which the ChIP-chip experiments did not have length bias

	YPD (135)	OC (72)	Unique TFs (YPD or OC) - (162)
1	ABF1	ARG81	A1#(MATA1)
2	ABT1	ARO80	ABF1
3	ACA1	BAS1	ABT1
4	AFT2	CHA4	ACA1
5	ARG80	GAT1	ADR1
6	ARG81	MET28	AFT2
7	ARO80	MET31	ARG80
8	ARR1	MET32	ARG81
9	ASH1	MET4	ARO80
10	ASK10	MOT3	ARR1
11	BAS1	PUT3	ASH1
12	BYE1	RPH1	ASK10
13	CAD1	RTG1	BAS1
14	CBF1	SIP4	BYE1
15	CHA4	DAL80	CAD1
16	CRZ1	GAT1	CBF1
17	CST6	GLN3	CHA4
18	CUP9	GZF3	CRZ1
19	DAL80	HAP2	CST6
20	DAL81	MSN2	CUP9
21	DAL82	MSN4	DAL80
22	DAT1	RTG1	DAL81
23	DOT6	RTG3	DAL82
24	ECM22	UGA3	DAT1
25	FHL1	AFT2	DIG1
26	FZF1	CAD1	DOT6
27	GAL3	GZF3	ECM22
28	GAL4	IME1	FHL1
29	GAL80	IME4	FZF1
30	GAT1	MAC1	GAL3
31	GCR1	MAL33	GAL4
32	GCR2	MIG2	GAL80
33	GLN3	RDS1	GAT1
34	GZF3	REB1	GAT1
35	HAA1	RIM101	GCR1
36	HAL9	RPN4#	GCR2
37	HAP2	SFP1	GLN3
38	HAP3	SIG1	GZF3
39	HAP5	YAP3	HAA1
40	HIR1	YAP5	HAL9
41	HIR2	YJL206C	HAP2
42	HIR3	HAP4	HAP3
43	HMS1	MSN2	HAP4
44	HMS2	MSN4	HAP5
45	HOG1	PDR1	HIR1
46	HSF1	PHO2	HIR2
47	IFH1	PUT3	HIR3
48	IME1	RCS1	HMS1
49	IME4	RIM101	HMS2
50	INO2	ROX1	HOG1
51	IXR1	RPH1	HSF1

52	KRE33	KSS1	IFH1
53	LEU3	TEC1	IME1
54	MAL33	DIG1	IME4
55	MBF1	MSS11	INO2
56	MET18	PHD1	IXR1
57	MET28	RLM1	KRE33
58	MET31	TEC1	KSS1
59	MET32	KSS1	LEU3
60	MIG1	THI2	MAC1
61	MIG2	GAL4	MAL33
62	MIG3	MIG1	MBF1
63	MOT3	RGT1	MET18
64	MSN1	ADR1	MET28
65	MSS11	GAT1	MET31
66	NDT80	HSF1	MET32
67	NNF2	MSN2	MET4
68	OAF1	SKN7	MIG1
69	OPI1	YAP1	MIG2
70	PDC2	PHO2	MIG3
71	PDR3	PHO4	MOT3
72	PIP2	GAL4	MSN1
73	PPR1		MSN2
74	RCO1		MSN4
75	RCS1		MSS11
76	RDR1		NDT80
77	RDS1		NNF2
78	RFX1		OAF1
79	RGT1		OPI1
80	RLR1		PDC2
81	RPH1		PDR1
82	RPI1		PDR3
83	RTS2		PHD1
84	SIG1		PHO2
85	SIP3		PHO4
86	SIP4		PIP2
87	SMK1		PPR1
88	SNF1		PUT3
89	SOK2		RCO1
90	SPT10		RCS1
91	SPT2		RDR1
92	SPT23		RDS1
93	SRD1		REB1
94	STB1		RFX1
95	STB4		RGT1
96	STB5		RIM101
97	STB6		RLM1
98	STP1		RLR1
99	STP2		ROX1
100	SUM1		RPH1
101	SUT2		RPH1
102	TBS1		RPI1
103	TEC1		RPN4#
104	THI2		RTG1
105	TOS8		RTG3
106	UGA3		RTS2
107	USV1		SFP1

108	WAR1	SIG1
109	WTM1	SIP3
110	WTM2	SIP4
111	XBP1	SKN7
112	YAP7	SMK1
113	YBL054W	SNF1
114	YBR267W	SOK2
115	YDR026c	SPT10
116	YDR049W	SPT2
117	YDR266c	SPT23
118	YDR520C	SRD1
119	YER130C	STB1
120	YER184C	STB4
121	YFL044C	STB5
122	YFL052w	STB6
123	YGR067C	STP1
124	YHP1	STP2
125	YJL206C	SUM1
126	YKL222C	SUT2
127	YKR064W	TBS1
128	YML081W	TEC1
129	YNR063W	THI2
130	YOX1	TOS8
131	YPR022C	UGA3
132	YRR1	USV1
133	ZAP1	WAR1
134	ZMS1	WTM1
135	A1#(MATA1)	WTM2
136		XBP1
137		YAP1
138		YAP3
139		YAP5
140		YAP7
141		YBL054W
142		YBR267W
143		YDR026c
144		YDR049W
145		YDR266c
146		YDR520C
147		YER130C
148		YER184C
149		YFL044C
150		YFL052w
151		YGR067C
152		YHP1
153		YJL206C
154		YKL222C
155		YKR064W
156		YML081W
157		YNR063W
158		YOX1
159		YPR022C
160		YRR1
161		ZAP1
162		ZMS1

Table S2

The motif predictions of DRIM on the Harbison filtered dataset.

Results of DRIM on the Harbison filtered dataset

TF	Motif	corrected mHG p-value
ABF1	NNHCGTNNDWRRTGAYNN	7.190E-117
ABF1	RTGATA	1.600E-14
ABF1	RTMACTDNDDACGANDH	2.030E-24
ABF1	RTMACTDNDDACGANDH	3.530E-17
ABT1*	AASAGR	5.970E-04
ACE2	CACACA	9.224E-09
AFT2	ACCTAC	1.610E-05
AFT2_H2O2Hi	ACACACACACACA	6.310E-22
ARG81	MRVSRSGAGTCRMDAR	5.270E-05
ARG81_SM	DNNDNGAGYCANNNNH	2.350E-05
ARG81_SM	CGCTAY	1.440E-04
ARG81_SM	AWTWGA	1.370E-03
ARG81_SM	NHNGAGTCANDH	5.890E-06
ARO80	WWNCCGANRNWNNCCGNRRNNW	1.000E-11
ARR1	ACACACACACACACACACACA	4.020E-07
ARR1	WTNATAA	1.690E-05
ASH1	NNNNDCGCGYCDBNNN	4.710E-15
ASH1	CCWCGW	2.100E-10
ASH1	CWGYGC	2.870E-10
ASH1	MYNCGAMGCGVSD	1.020E-14
BAS1	NMVGAGTCADNN	6.160E-16
BAS1_SM	YGACTC	1.380E-05
BAS1_SM	NHRGAGTCAKNN	1.980E-07
CAD1	CTAWRCA	6.130E-04
CAD1_H2O2Hi	AASCAW	7.190E-04
CBF1	CACGTG	5.610E-76
CBF1	NNNCACGTGAYHNNNN	6.150E-78
CBF1	NDKCACGTGAYHND	5.160E-52
CBF1	DKCACGTGAYHDN	1.810E-48
CRZ1	YRNCGCVNMDTNTDBNNNDACGHHH	1.930E-12
CRZ1	NNNDNCRTGGYDNNNN	2.840E-07
CRZ1	CACNCAC	1.250E-06
CRZ1	DHRCGCBHNVAAGDVV	8.820E-11
DAL81	HBVCACGGCDVN	1.450E-09
DAL81	CARAAR	2.820E-04
DAL81	ACGNCGC	6.670E-06
DAT1	CTRCGCTTAGCCT	8.700E-06
DIG1_BUT14	CATTCY	1.180E-12
DIG1_BUT14	RAGAATG	1.920E-13
DIG1_BUT14	GTTTCANNW	4.530E-11
DIG1_BUT14	CTGCRS	2.770E-07
DOT6	YCCGRC	8.610E-07
DOT6	STTGSC	8.710E-05
DOT6	CGSGSC	8.400E-05
DOT6	NGCCGGR	3.700E-06
FHL1	WNMAYCCRTACAYHH	1.350E-61
FHL1	NNHHNCAYCCRWNNAN	4.710E-51
FHL1	MAYCCRWACATHH	3.180E-75
FHL1	MAYCCGTACAYH	6.750E-50

GAL4	CGGNNNNNNNNNNNCGA	9.120E-07
GAL4_GAL	CGGNNNNNNNNNNNCCG	3.830E-11
GAL4_RAFF	CGGNNNNNNNNNNNCCG	1.070E-12
GAL4_RAFF	CGGSGS	5.020E-06
GAL4_RAFF	CYGASC	1.240E-04
GAL4_RAFF	DNHCGGMNNAGANDH	3.200E-06
GAT1	CRGRCG	1.590E-11
GAT1	AGCRRC	6.420E-09
GAT1	CCRCYC	2.320E-09
GAT1	RRGAGC	2.780E-08
GAT1_RAPA	HHNCTTATCWNH	4.720E-09
GAT1_RAPA	YCTTATC	4.240E-07
GAT1_SM	RAWATC	3.170E-04
GAT1_SM	AATNNNNNNNNNNNNNGTA	5.590E-06
GCR1	NDDNWYGACCCNNVHV	1.600E-04
GCR1	CTGNNNNNNNNNCCC	1.930E-05
GCR2	ACANNCAC	4.020E-06
GLN3	AASTYT	1.210E-05
GLN3	AATSTS	5.910E-05
GLN3	GWTTYA	5.340E-05
GLN3	SAYCTA	2.590E-04
GLN3_RAPA	CTTATC	1.010E-15
GLN3_RAPA	AYCTAA	2.210E-05
GLN3_RAPA	DHDATAWGAGDH	9.680E-08
GLN3_RAPA	SRATTA	1.810E-04
HAA1	AATSTY	9.450E-05
HAA1	WGAAAR	4.260E-04
HAA1	WNTTTTC	3.920E-06
HAP2_RAPA	DDCCAATCR	5.220E-07
HAP3	AAWCTW	5.490E-04
HAP3	AARTAC	5.420E-04
HAP4_H2O2Lo	ATSTTS	8.060E-05
HIR1	AWAATW	1.110E-05
HIR1	ATWTTR	8.220E-05
HIR1	ARTSAT	3.880E-04
HIR3	ATTTWR	3.850E-07
HIR3	CRATAW	3.620E-04
HIR3	TGANNNNNNNTCA	1.510E-05
HMS2	YYTCAA	1.650E-05
HMS2	AAWYTC	2.130E-05
HMS2	RCTTWC	5.710E-04
HMS2	AGAASG	3.330E-04
HOG1	NDDNDWAWTAADNNDD	4.500E-10
HOG1	TAANNNNNNNTTA	7.930E-06
IME1_H2O2Hi	CGGCCG	1.200E-07
IME4	ACACACACACACA	8.020E-20
IME4_H2O2Hi	AARTTR	8.780E-05
IME4_H2O2Hi	TWTSAA	2.320E-04
IME4_H2O2Hi	ATGNNNNNNAAT	1.510E-05
IME4_H2O2Hi	NDNAATNHHNNNHNNDHNNTTCNNN	4.960E-06
INO2	CACRTG	1.570E-19
INO2	CACATG	6.370E-18
INO2	CSTGSG	9.860E-07
INO2	NHNGCAHRTGADNW	7.290E-09
IXR1	DNCAGVWNDNNWNNNNHNVCCANNW	5.410E-06
KSS1_Alpha	AGRARA	4.050E-06

LEU3	CCGNNNCCG	7.020E-10
LEU3	WTTAAC	2.040E-06
LEU3	NDCCGGWACCGGM	4.160E-09
LEU3	RTTGRA	2.830E-04
MAL33_H2O2Hi	ACACACACACACA	4.760E-28
MAL33_H2O2Hi	ACACAC	3.070E-20
MAL33_H2O2Hi	CACNNNNNNNCAC	8.400E-21
MAL33_H2O2Hi	CACACACACACACACA	2.000E-20
MET31	DNKCACGTGAWNWN	1.529E-04
MET31	GGNGCCAC	1.000E-03
MET32	CACGTG	5.640E-09
MET32	SSGCCACA	4.700E-05
MET32_SM	CACGTG	3.230E-07
MET32_SM	SSGCCACA	3.230E-04
MET4_SM	NCWCGTGA	4.170E-06
MET4_SM	GGNGCCAC	4.130E-04
MIG1	TRAGYA	7.330E-04
MIG1	VMHWHCCCCACNHWHV	1.790E-05
MIG1	WACYCC	7.930E-04
MOT3_SM	CCASRG	9.010E-04
MSN2_H2O2Lo	NNNNBCYRGCCNDNHN	1.840E-07
MSN2_H2O2Lo	NNNHNCCCCTRHDNHH	1.140E-07
MSN2_H2O2Lo	CAGGGG	1.700E-06
MSN2_H2O2Lo	GCCNNNCCA	4.820E-06
OAF1	AARGAW	4.050E-04
OAF1	DNNCCADCGCHNN	1.120E-09
OAF1	RSCGCA	4.560E-04
OAF1	NVNCGCNNHNHNGGCHNN	7.350E-07
PHO4_Pi-	NBMACGTGCNNN	3.040E-19
PHO4_Pi-	CRCGSG	1.240E-09
PHO4_Pi-	TWSGCA	3.350E-07
PHO4_Pi-	NNDNNCGTRGRNNHNN	3.800E-07
PUT3_H2O2Lo	RCACCY	1.290E-24
PUT3_H2O2Lo	WHKGCACCCNNN	2.050E-24
PUT3_H2O2Lo	SGCACW	3.990E-08
PUT3_H2O2Lo	STWCAC	2.740E-06
RCS1_H2O2Lo	NKNCGGGTAAYN	1.620E-117
RCS1_H2O2Lo	HNNNNRTTACCYKNHN	3.810E-84
RCS1_H2O2Lo	DNMGGGTAAYNND	1.750E-103
RCS1_H2O2Lo	HNKCCGGGTAAYNN	1.510E-54
RDS1_H2O2Hi	HBKCGGCCGAVNN	2.570E-13
RDS1_H2O2Hi	DNHBKCGGCCGAVDBD	1.440E-08
RDS1_H2O2Hi	YTWGAA	2.370E-04
RDS1_H2O2Hi	RWTGTA	7.720E-04
REB1_H2O2Hi	DNMGGGTAAHNN	6.570E-58
REB1_H2O2Hi	NNNTWAYCCGGNNHNN	5.290E-25
REB1_H2O2Hi	DNDCCGGGTAANN	6.170E-25
REB1_H2O2Hi	CGGGSR	1.080E-09
RIM101_H2O2Hi	WTSAAA	1.360E-05
RIM101_H2O2Hi	AATNNNNATC	7.510E-06
RIM101_H2O2Hi	AGASTS	5.000E-04
RIM101_H2O2Hi	SRAGTA	5.450E-04
RIM101_H2O2Lo	NHNNKCGTRCANNNNN	5.090E-07
RIM101_H2O2Lo	CCCNNNNNNNNNNTGC	1.520E-07
RIM101_H2O2Lo	WRGTGC	9.040E-06
RIM101_H2O2Lo	ACGGAG	2.640E-07

RPH1_H2O2Lo	YWTCAA	2.650E-04
RPH1_SM	TAARWA	4.840E-05
RPH1_SM	RTCCAW	6.580E-04
RPI1	AAGTYC	7.080E-05
RTG1_RAPA	AATNNNNNNNNTTA	2.140E-06
RTG1_RAPA	CAATAY	6.590E-05
RTG1_RAPA	WASTAC	2.350E-04
RTG1_RAPA	AATNCTA	1.750E-05
RTG3_RAPA	NNDNNCRTGACHNNNH	2.490E-05
RTG3_RAPA	NNNAGTCATNHN	3.230E-06
SFP1_H2O2Hi	CACNNNNNCAC	2.040E-05
SIP4_SM	AWTART	5.610E-06
SIP4_SM	AATNNNTGA	4.150E-07
SIP4_SM	AWCATR	1.540E-05
SIP4_SM	GAAYYA	4.190E-05
SKN7_HEAT	BNVNNYGGGCCNNVNN	1.700E-12
SKN7_HEAT	NNVCGGGCCNNN	2.940E-12
SKN7_HEAT	CCGWGY	7.130E-08
SKN7_HEAT	CGCNGCC	9.540E-08
SNF1	ATTTSY	2.900E-04
SOK2	YAGGCA	5.280E-10
SOK2	CSTGCA	1.910E-09
SOK2	CWWAGA	2.770E-08
SOK2	NNNNNYGCRGANNNNN	1.650E-08
SPT23	AWTYTA	1.640E-04
SPT23	ATSTTY	2.340E-04
SPT23	ATWARA	4.780E-04
STB1	CGCGAR	3.540E-08
STB1	VDDCGCGAAAWN	1.490E-10
STB1	RNNCGCSAAAADHH	1.190E-10
STB1	NNNAAACGCDNV	2.570E-06
STB4	HYTCGGVYCGAVDB	3.420E-09
STB4	HHDNHTYCARANHHNN	1.310E-06
STB4	DDDNNCRATTRNNNDN	4.770E-07
STB4	TAANNNNNNNGCA	2.750E-06
STB5	NVDCGGNVTTAHRV	3.350E-11
STB5	HNNNNAYARCTNNNNN	5.540E-05
STB6	ATANNNNNNTGG	6.720E-07
STP1	GGCNNNNNNNNNNNNNNAAA	1.520E-05
STP2	GWARAA	4.910E-04
SUM1	NNNHHGYGTCABHDHH	4.150E-15
SUM1	WWWGTGTCABHW	6.450E-10
SUM1	GTWACA	3.790E-05
SUM1	AWTTWA	5.180E-04
TBS1	RWGGAA	2.950E-05
TBS1	YSTTTA	6.000E-05
TBS1	ACATTS	4.790E-05
TBS1	CAWAAW	1.700E-05
TEC1	DNHHNCATTCYNNNNH	3.830E-10
TEC1	NNNAGAATGNDD	1.390E-08
TEC1_Alpha	HNNGTTTCADHN	1.170E-09
TEC1_Alpha	NNHACATTCNNN	2.670E-07
THI2_Thi-	ACGNNNNNNNNNNNNNNNTAT	2.640E-05
TOS8	CCCNNCCA	3.090E-05
UGA3_RAPA	WTWAAA	5.820E-05
UGA3_RAPA	SAYTTA	6.190E-04

YAP3_H2O2Hi	TCAWRA	6.730E-05
YAP3_H2O2Hi	AARRTG	7.410E-04
YAP3_H2O2Hi	ASTAWC	3.220E-04
YAP5_H2O2Hi	AATNNNNNNNNNNNATT	1.110E-11
YAP5_H2O2Hi	AATWYA	1.470E-09
YAP5_H2O2Hi	ATTSTR	1.860E-07
YAP5_H2O2Hi	ATYARA	7.840E-07
YAP7	CSTTTY	2.850E-04
YBR267W	ATTYTS	9.350E-06
YBR267W	SGSAAA	9.350E-04
YBR267W	YSTTTC	8.430E-04
YBR267W	RRATAA	5.380E-04
YDR026c	TTTACCCGGMNH	9.230E-30
YDR026c	DNKCCGGGTAAADW	2.740E-19
YDR026c	WNDMMGGGTAAWNNNH	1.630E-14
YDR049W	CAYTTY	8.840E-05
YDR266c	AYAYCT	7.280E-04
YFL052w	WCWTGA	5.200E-04
YJL206C	CCCGWY	8.970E-05
YKR064W	MDVCGGADTTAWBV	3.480E-07
YOX1	ATTTWR	3.390E-04
YOX1	TRTTRA	1.740E-04
YOX1	AATDNNNDDNHNNDHHTTAH	7.090E-06

Table S3

A Comparison between the predictions of DRIM and those reported in [1] .

TFs for which Harbison and DRIM predict the same motif	TFs for which DRIM and Harbison predictions are different	TFs for which Harbison predicts and DRIM does not
27	5	11
ABF1	HAP4	DAL82
AFT2	SFP1	HSF1
CAD1	SIP4	PDR1
BAS1	THI2	PHD1
CBF1	YAP7	PHO2
DIG1		RFX1
FHL1		RLR1
GAL4		SIG1
GAT1		SPT2
GLN3		YAP1
INO2		ZAP1
LEU3		
MET4		
MSN2		
PHO4		
RCS1		
RDS1		
REB1		
SKN7		
SOK2		
SPT23		
STB1		
STB4		
STB5		
TEC1		
YDR026c		
SUM1		

Table S4

A Comparison between mHG flexible cutoffs and 10^{-3} fixed cutoffs in yeast ChIP-chip data.

Comparison between the number of promoters for which the binding signal < 10–3 (denoted #(10–3)) with the number of promoters at which mHG was attained in yeast ChIP-chip data.

TF name	fixed #p<0.001	mHG optimal threshold
ABF1	180	97
AFT2	20	97
AFT2H2O2hi	51	90
BAS1	39	87
CBF1	10	93
FHL1	133	99
GAL4	16	19
GAT1	8	99
GLN3_RAPA	79	57
HAP3	30	67
INO2	36	19
Leu3	31	22
MSN_H2O2Lo	74	99
SOK2	0	75
STB1	22	15
SUM1	54	92
TEC1	37	85
YDR026c	16	69
RDS1_H2O2Hi	52	45
REB1_H2O2hi	49	87

8 Appendix II - List of publications (during M.Sc. period):

- Eran Eden, Doron Lipson, Sivan Yogev and Zohar Yakhini. Discovering Sequence Motifs in Ranked Lists of DNA Seqeunces. *PLoS Computational Biology*, 2007.

- Yeshayahu Schlesinger, Ravid Straussman, Ilana Keshet, Shlomit Farkash, Merav Hecht, Joseph Zimmerman, Eran Eden, Zohar Yakhini, Etti Ben-Shushan, Benjamin E Reubinoff, Yehudit Bergman, Itamar Simon, Howard Cedar. Polycomb mediated histone H3(K27) methylation pre-marks genes for de-novo methylation in cancer. *Nature Genetics*, 2007

- Eran Eden, Michael Rudzsky, Vera Brod, Dan Waisman, Haim Bitterman, Edmond Sabo and Ehud Rivlin. An automated method for analysis of blood cell flow characteristics from in-vivo video-microscopic studies. *IEEE, Transactions on Medical Imaging*, vol. 24 Issue: 8, pp. 1011- 1024, 2005.

9 Appendix III - Web servers and software (during M.Sc. period):

- *DRIM* - the software is publicly available via an easy to use web interface: http://bioinfo.cs.technion.ac.il/drim. Due to running time considerations the web service has restrictions on the number and length of the DNA sequences in the query. The exhaustive motif search space is also restricted. These restrictions can be removed by downloading a local copy of DRIM. For more details please see website.

- *GOviz* - the mHG based GO analysis and graphical visualization tool is available via the following web interface: http://bioinfo.cs.technion.ac.il/GOviz

- *SimTree* - a tool for comparing RNA secondary structures is available via the following web interface: http://bioinfo.cs.technion.ac.il/SimTree/